

September 24, 2009

**An exchange–Coulomb model potential energy surface for the
Ne–CO interaction. II. Molecular beam scattering and bulk gas
phenomena in Ne–CO mixtures.**

Ashok K. Dham

Department of Physics, Punjabi University, Patiala, 147002, India

George C. McBane

Department of Chemistry, Grand Valley State University, Allendale, MI 49401 USA

Frederick R. W. McCourt

Department of Chemistry, University of Waterloo,

Waterloo, Ontario, Canada N2L 3G1

William J. Meath

Department of Chemistry, University of Western Ontario,

London, Ontario, Canada N6A 5B7

Abstract

Four potential energy surfaces are of current interest for the Ne–CO interaction. Two are high-level fully ab initio surfaces obtained a decade ago using symmetry-adapted perturbation theory and supermolecule coupled-cluster methods. The other two are very recent exchange-Coulomb model potential energy surfaces constructed by using ab initio Heitler–London interaction energies and literature long range dispersion and induction energies, followed by the determination of a small number of adjustable parameters to reproduce a selected subset of pure rotational transition frequencies for the $^{20}\text{Ne}\text{--}^{12}\text{C}^{16}\text{O}$ van der Waals cluster. Testing of the four potential energy surfaces against a wide range of available experimental microwave, millimeter-wave and mid-infrared Ne–CO transition frequencies indicated that the XC potential energy surfaces gave results that were generally far superior to the earlier fully ab initio surfaces. In this paper, two XC model surfaces and the two fully ab initio surfaces are tested for their abilities to reproduce experiment for a wide range of non-spectroscopic Ne–CO gas mixture properties. The properties considered here are: relative integral cross sections and the angle dependence of rotational state-to-state differential cross sections, rotational relaxation rate constants for $\text{CO}(v=2)$ in Ne–CO mixtures at $T = 296$ K, pressure broadening of two pure rotational lines and of the rovibrational lines in the CO fundamental and first overtone transitions at 300 K, and the temperature and, where appropriate, mole fraction dependencies of the interaction second virial coefficient, the binary diffusion coefficient, the interaction viscosity, the mixture shear viscosity and thermal conductivity coefficients, and the thermal diffusion factor. The XC model potential energy surfaces give results that lie within or very nearly within the experimental uncertainties for all properties considered, while the coupled-cluster ab initio surface gives results that agree similarly well for all but one of the properties considered. When the present comparisons are combined with the ability to give accurate spectroscopic transi-

tion frequencies for the Ne–CO van der Waals complex, only the XC potential energy surfaces give results that agree well with all extant experimental data for the Ne–CO interaction.

I. INTRODUCTION

The exchange–Coulomb (XC) potential energy model was originally developed to give a simple method for constructing reliable potential energies between closed-shell atoms or for representing the spherical part of potential energy surfaces (PESs) for interactions involving molecules (see Refs. 1–4 and references therein) and later modified to provide forms more suitable for interactions involving molecules (see Refs. 4–9 and references therein). By fitting a small number of adjustable parameters in the XC model PES to a selected set of pure rotational transition frequencies^{10–13} of the $^{20}\text{Ne}-^{12}\text{C}^{16}\text{O}$ cluster, a set of XC surfaces has recently been developed⁹ for the Ne–CO interaction. One of these PESs, denoted $\text{XC}(\text{fit})_{r=r_e}$, is a rigid-rotor PES in which the CO bond length r is fixed at its experimental spectroscopic equilibrium value r_e , while another, denoted $\overline{\text{XC}(\text{fit})}_{v_{\text{CO}}=0}$, has been obtained by averaging the stretching dependence over the ground vibrational state of the CO molecule.

Two high-level ab initio Ne–CO surfaces, one obtained¹⁴ from symmetry adapted perturbation theory (SAPT) calculations, the other obtained¹⁵ from supermolecule coupled-cluster calculations at the singles, doubles, and perturbative triples, or CCSD(T), level of approximation, have been published. They were referred to, respectively, as the SAPT and S2 PESs in Ref. 9. The same convention is employed here. In both cases analytical fits to the ab initio points have been made available.

The XC(fit) surfaces have been shown⁹ to give results for the wide range of available experimental microwave¹⁰ (MW), millimeter-wave^{11–13} (MMW) and mid-infrared^{16,17} (IR) NeCO transition frequencies that are generally far superior to those obtained using the SAPT and S2 surfaces. The main purpose of the present paper is to test how well calculations employing the XC surfaces reproduce experiment for a wide range of non-spectroscopic Ne–

CO gas mixture properties and to compare how the XC surfaces fare relative to the SAPT and S2 surfaces. The relative importance of the average stretching dependence in the XC surfaces for the calculation of accurate molecular beam and bulk gas phenomena is also examined, as is the reliability of relatively inexpensive Mason–Monchick¹⁸ approximation calculations of diffusion and shear viscosity coefficients for dilute gases.

Both beam scattering (microscopic) and bulk mixture properties are utilized to help discriminate between the XC(fit) surfaces developed in Ref. 9 and the SAPT and S2 surfaces reported in Refs. 14 and 15. Specifically, relative integral cross sections¹⁹ and the angle-dependence of the differential cross sections²⁰ for state-to-state rotational energy transfer are employed at the microscopic level, and pressure broadening,^{21–24} state-to-state rotational energy transfer rate coefficients,²⁵ the temperature dependence of the interaction second virial coefficient,^{26,27} and four binary mixture transport coefficients, specifically diffusion,²⁸ shear viscosity,²⁹ thermal conductivity,³⁰ and thermal diffusion,²⁸ are employed at the bulk level. The calculation of these properties and their comparisons with experiment augments previous studies^{15,19,20,25} of the utility of the S2 and SAPT surfaces for the computation of state-to-state differential and integral molecular beam scattering cross sections, pressure broadening of the CO $1 \leftarrow 0$ rotational transition, rotational energy transfer rate coefficients, and interaction second virial coefficients.

Section II gives a brief summary of the XC(fit) model surfaces developed in Ref. 9, while Section III presents a comparison between the experimental microscopic phenomena and the corresponding quantities calculated from the $\text{XC(fit)}_{r=r_e}$, $\overline{\text{XC(fit)}}_{v_{\text{CO}}=0}$, SAPT, and S2 surfaces. Similarly, Section IV presents a comparison for the various macroscopic phenomena. Finally, Section V contains an overall summary of the results obtained, together with some

conclusions that can be drawn from them. In particular, while the two Ne–CO XC surfaces of Ref. 9 provide the best overall representation of the Ne–CO interaction currently available, the SAPT ab initio PES of Ref. 14, and especially the S2 ab initio PES of Ref. 15, often do rather well in predicting molecular beam scattering and/or bulk gas phenomena.

II. THE XC(FIT) MODEL POTENTIAL ENERGY SURFACES.

The two recently developed⁹ XC model PESs both have the basic XC form

$$V(R, \theta) = F(\theta)E_{\text{HL}}^{(1)}(R, \theta) + \Delta E_C(R, \theta), \quad (1)$$

in which R is the distance from the diatom center-of-mass to the atom and θ gives the orientation of the diatom relative to the interspecies axis \mathbf{R} of the complex (such that the alignment Ne–C–O corresponds to $\theta = 0$). The model for the mostly-repulsive part of the PES is given by the Heitler–London interaction energy, $E_{\text{HL}}^{(1)}$, multiplied by a function F that is represented by a simple Legendre expansion involving θ only. The mostly-attractive part of the model PES, given by

$$\Delta E_C = -G_{10}(R, \theta) \sum_{n=6}^{10} f_n(R, \theta) C_n(R, \theta) R^{-n}, \quad (2)$$

is represented by an individually damped, overall corrected, dispersion-plus-induction energy series through order R^{-10} . The individual damping functions, $f_n(R, \theta)$, and the overall corrector function, $G_{10}(R, \theta)$, are obtained from those^{3,4,31,32} for the prototypical non-bonded H–H($\alpha^3\Sigma_u^+$) interaction by multiplying R by the scale factor $S(\theta) = 7.82/R_e(\theta)$, with 7.82 a_0 being the internuclear distance corresponding to the potential energy minimum for H–

$H(a^3\Sigma_u^+)$, while $R_e(\theta)$ is the equilibrium interspecies distance for Ne–CO at orientation θ . The flexibility in the XC potential energy model is provided by parameters in the function F and through varying the composite multipolar long range interaction energy coefficients $C_n(R, \theta)$ within their estimated uncertainties. The initial⁹ XC PES is a three-dimensional PES, denoted 3DXC(0), in which the Heitler–London energy has been calculated as a function of R , θ , and the CO bond distance r with relatively high quality SCF wavefunctions for the isolated species, then fitted to a convenient functional form, and ΔE_C is constructed by using the most reliable literature values^{33–36} for the stretching dependence of the dispersion and induction energies, which have been fitted to a simple polynomial in a CO stretching coordinate. The rigid-rotor PES is obtained by setting $r = r_e$ in the 3DXC(0) PES, while the vibrationally-averaged PES is obtained by averaging the 3DXC(0) PES over the ground vibrational state of the CO molecule; in each case a final determination of the adjustable parameters in the resulting PESs is made by fitting to accurate experimental values for a set of spectroscopic transition frequencies for the $^{20}\text{Ne}-^{12}\text{C}^{16}\text{O}$ cluster. Nine MW frequencies were employed for the $\text{XC}(\text{fit})_{r=r_e}$ PES, while four MW frequencies and three MMW frequencies were employed for the $\overline{\text{XC}(\text{fit})}_{v_{\text{CO}}=0}$ PES.

III. MICROSCOPIC PHENOMENA

Relative state-to-state differential²⁰ and integral¹⁹ scattering cross sections have been measured for Ne-CO rotational excitation at energies in the range 500–800 cm^{-1} . Both types of scattering cross section are determined mainly by the shape and steepness of the repulsive wall. Neither is very sensitive to the absolute size of the repulsive wall because of the relative nature of the measurements.

Contours at three relevant energies on the repulsive wall are shown for three PESs in Fig. 1. The $\text{XC}(\text{fit})_{r=r_e}$ PES and the S2 PES behave very similarly for Ne approaching the carbon end of the CO molecule, while the SAPT wall extends about $0.09 a_0$ farther at that end. When Ne approaches the waist of the CO molecule, all three surfaces behave similarly, but the $\text{XC}(\text{fit})_{r=r_e}$ PES and the SAPT PES both permit the Ne atom to approach about $0.04 a_0$ more closely than does the S2 PES. At the oxygen end of the CO molecule, the S2 and SAPT surfaces permit a $0.03 a_0$ closer approach of the Ne atom than does the $\text{XC}(\text{fit})_{r=r_e}$ PES. Overall, the SAPT PES is the most anisotropic of the three surfaces, and the S2 PES is least anisotropic. The similar appearance of the sets of contours at the three different energies indicates that the steepness of the wall is much the same for each PES.

A. Molecular beam state-to-state differential scattering cross sections

The state-to-state differential cross sections reported by Lorenz *et al.*²⁰ provide the most discriminating experimental test of the shape of the repulsive wall below about 600 cm^{-1} . Those data are also relatively straightforward to interpret: the main carbon-end rotational rainbow maximum moves to lower scattering angle as the potential anisotropy increases. The SAPT PES predicts those maxima to appear at consistently smaller scattering angles than does the S2 PES; the comparisons presented in Ref. 20 indicated that the predictions of the S2 PES gave better agreement. Computations of the differential cross sections from the $\text{XC}(\text{fit})_{r=r_e}$ PES are reported herein, and comparisons are made with the same experimental data. Results obtained for the other two potential energy surfaces have also been included for ease of comparison.

Accurate close-coupled (CC) values of the cross sections have been computed with

the MOLSCAT program of Hutson and Green³⁷ using the Alexander and Manolopoulos propagator³⁸ to solve the coupled equations. The angular expansion of the potential included 14 Legendre terms, with expansion coefficients determined by a 20-point Gaussian quadrature using the standard VRTP mechanism of MOLSCAT. Rotational states of CO through $j = 21$ were included in the channel basis and total angular momenta up to $J = 140$ were included in the partial wave sums.

To match the experimental collision energy distribution, calculations at energies 467.7, 511.0, and 554.3 cm^{-1} were averaged with a three-point Gauss-Hermite quadrature. The differential cross sections were averaged over the initial rotational populations of the experiment, namely, 77% $j = 0$, 23% $j = 1$. All calculations have been performed for the $^{12}\text{C}^{16}\text{O}$ isotopologue, since the experiment employed mass-selective detection. Moreover, for consistency with previous work, only the ^{20}Ne isotope has been considered, to give a corresponding Ne-CO reduced mass of 11.6632 amu. Figure 2 displays results obtained for the $\text{XC}(\text{fit})_{r=r_e}$ PES for a representative set of final rotational states j_f , together with comparable results for the SAPT and S2 PESs. Similar calculations using the average Ne atomic mass produced differential cross sections that differ very slightly from those shown in Fig. 2.

The differential cross sections predicted by the $\text{XC}(\text{fit})_{r=r_e}$ PES lie between those obtained from the SAPT and S2 PESs, as can be expected, and are generally closer to the cross sections obtained from the S2 PES. Both the $\text{XC}(\text{fit})_{r=r_e}$ and S2 calculations agree better with the data than do the SAPT calculations, especially in their predictions of the position of the C-end rotational rainbow. The trends are consistent with the discussion of the repulsive wall shapes above; because the wall of the SAPT PES extends further from the CO center-of-mass at the carbon end, rotational excitation caused by collisions at that end of the CO molecule

requires lower scattering angles when the SAPT PES is employed.

At low and intermediate final j values, the rainbow structures predicted by the S2 PES are somewhat closer to the experimental structures than are those calculated with the $\text{XC}(\text{fit})_{r=r_e}$ PES. However, for $j_f > 12$, the $\text{XC}(\text{fit})_{r=r_e}$ PES appears to provide better overall agreement with experiment. These differences are likely within the experimental error limits; the uncertainty in the extracted angular positions was reported by Lorenz *et al.*²⁰ to be about 2° , the uncertainty in the peak of the collision energy distribution to be 15 cm^{-1} . These two uncertainties could shift the experimental curves sufficiently to favor either the $\text{XC}(\text{fit})_{r=r_e}$ or S2 surfaces, so that the experimental data are unable to distinguish between them.

Scattering calculations have also been carried out using a stretching-dependent XC PES vibrationally averaged over the $v_{\text{CO}} = 0$ vibrational motion. The results obtained using this PES,⁹ denoted $\overline{\text{XC}(\text{fit})}_{v_{\text{CO}}=0}$, are essentially indistinguishable from the $\text{XC}(\text{fit})_{r=r_e}$ curves shown in Fig. 2.

During the preparation of the present paper, an error was discovered in Ref. 20 : in Fig. 3 of that paper, the plots for the theoretical differential cross sections were obtained from computations made for an average collision energy of 533 cm^{-1} , rather than for the energy 511 cm^{-1} stated there. This error had the effect of shifting the rainbow peaks to lower angle, thereby improving the apparent agreement with experiment for the S2 PES, but worsening it for the SAPT PES. This shift increases with final rotational state, and at $j_f = 13$ the shift is slightly less than 5° . The S2 PES still clearly provides better agreement with the experimental results, and consequently none of the physical conclusions given in Ref. 20 requires modification. Fig. 2 shows results obtained for the $\text{XC}(\text{fit})_{r=r_e}$, S2, and SAPT surfaces at average collision energy 511 cm^{-1} .

B. State-to-state integral scattering cross sections

Antonova *et al.*¹⁹ reported relative product state densities for rotational excitation of CO by Ne at collision energies of 711 and 797 cm⁻¹. These densities are related to state-to-state integral cross sections by a density-to-flux transformation that depends both on the corresponding *differential* cross sections and on the geometry of the experiment. The necessary density-to-flux corrections have been computed for the XC(fit)_{r=r_e} PES for comparison with the experimental results of Ref. 19.

Figure 3 shows the experimental product densities at collision energies 711 and 797 cm⁻¹, together with corresponding values computed from the XC(fit)_{r=r_e} PES and product densities reported for the S2 PES in Ref. 19. The results for the XC(fit)_{r=r_e} PES have been computed using CC calculations in the manner described in the previous subsection, while the density-to-flux corrections, using CC differential cross sections from the XC(fit)_{r=r_e} PES, have been computed as described in Ref. 19. The present scattering calculations were carried out using the average Ne isotopic mass rather than an explicit average over the stable isotopes; as pointed out in the previous subsection, the consequent difference is negligible. Cross sections at each experimental collision energy have been averaged over the initial rotational populations (0.75 in $j = 0$ and 0.25 in $j = 1$) reported in Ref. 19.

The most interesting point of comparison between experiment and theory is the even-odd alternation in the observed densities between $j_f = 4$ and 11. This alternation is caused by an interference effect that appears because the same final j can be excited by collisions at either end of the CO molecule.^{39,40} In the experiment, there are clear maxima at $j_f = 5, 7,$ and 9 at lower energies, and a maximum at $j_f = 5$ and a sharp step down between $j_f = 7$ and 8 at higher energies. The preference for odd j_f , including a maximum at $j_f = 5$, is a

robust feature of CO–rare gas scattering. This preference also appears in similar He–CO scattering measurements of Antonova *et al.*⁴¹ and in independent measurements by Carty *et al.*⁴² of state-to-state rate coefficients for He–CO($v=2$) rotational energy transfer at 294 K.

The integral cross sections and product densities predicted by the $\text{XC}(\text{fit})_{r=r_e}$ PES are very similar to those predicted by the S2 PES. For both the $\text{XC}(\text{fit})_{r=r_e}$ and S2 potential energy surfaces, a clear maximum doesn't appear until $j_f = 7$ and persists until $j_f = 11$ at both collision energies. The oscillations therefore set in a little later, and persist a little longer, than in experiment.

The predictions of the $\text{XC}(\text{fit})_{r=r_e}$ and S2 surfaces are much more similar to one another than to experiment, so that, once again, comparison with experiment cannot distinguish between them. Both surfaces give the correct qualitative phase of the oscillations, i.e., they show a preference for odd j_f between 5 and 10, where the oscillations are clearest. Antonova *et al.*¹⁹ showed that the SAPT PES predicts maxima at $j_f = 4$ and 6, rather than at $j_f = 5$ and 7, but gives predictions that agree with the S2 PES (and also with the $\text{XC}(\text{fit})_{r=r_e}$ PES) for high j_f values.

As was the case for the state-to-state differential cross sections, calculations using the vibrationally averaged $\overline{\text{XC}(\text{fit})}_{v_{\text{CO}}=0}$ PES also gave results that are indistinguishable from those obtained using the rigid-rotor $\text{XC}(\text{fit})_{r=r_e}$ PES and shown in Figs. 3 and 4.

Figure 4 shows integral cross sections from the three surfaces for the $0 \rightarrow j_f$ excitation at 711 cm^{-1} to permit comparison of the calculated results for the three PESs in the absence of the rotational state distribution and the density-to-flux transformation. The difference in the predictions of the SAPT PES and those of the other two PESs for $4 \leq j_f \leq 7$ is clear. The upper panel of Figure 4 shows the density-to-flux factors computed from the $\text{XC}(\text{fit})_{r=r_e}$

PES at 711 cm^{-1} . These sensitivity factors cannot be the cause of the missing maximum at $j_f = 5$ in Fig. 3, since they are nearly constant over that region. Their main effect is to increase the experimental sensitivity to slow-moving high rotational states.

Another point of comparison between experiment and theory is in the rate of decrease of the relative densities with increasing j_f . As can be seen from Fig. 3 (comparing the S2 and $\text{XC}(\text{fit})_{r=r_e}$ PESs) and Fig. 3 of Ref. 19 (comparing the S2 and SAPT PESs), all three surfaces are in good agreement with one another, but show a slower decrease than does experiment. Antonova *et al.*¹⁹ have pointed out that this discrepancy may be due to polarization effects that were not taken into account during the experimental data analysis.

IV. MACROSCOPIC PHENOMENA

Bulk transport and relaxation phenomena, van der Waals spectra, and molecular beam scattering provide complementary data for the development and testing of PESs. Van der Waals spectra are sensitive mainly to features of the potential well, especially in the vicinity of the minimum in the PES, molecular beam scattering is largely sensitive to the shape of the repulsive wall of the PES at and below the beam energy, and bulk transport and relaxation phenomena, because they are determined by thermally-averaged collision cross sections, are sensitive to significant portions of the repulsive wall of the PES. Measurements of bulk phenomena over as large a temperature range as possible are thus desirable. Comparisons between calculated bulk gas mixture properties, such as the interaction second virial coefficient and transport and/or relaxation phenomena and available experimental data thus provide additional tests of the qualities of the $\text{XC}(\text{fit})_{r=r_e}$ and $\overline{\text{XC}(\text{fit})}_{v_{\text{CO}}=0}$ PESs obtained recently.⁹

Experimental data for Ne–CO binary mixtures are available for the interaction second virial coefficient^{26,27} over an extended temperature range (123 K–463 K), for the binary diffusion²⁸ and shear viscosity²⁹ coefficients over more limited temperature ranges (277 K–323 K and 298 K–473 K, respectively), and for the thermal conductivity coefficient³⁰ and the thermal diffusion factor²⁸ only at 300 K. Binary diffusion (mass transport) and shear viscosity (momentum transport) are determined largely by elastic collisions, so that they, like the second virial coefficient, are dominated by the isotropic component of the PES. Because thermal conductivity and thermal diffusion have contributions that are associated with the transport of (molecular) internal energy and have larger inelastic collisional contributions than do diffusion and shear viscosity, they are slightly more sensitive to the anisotropic components of a PES. However, the thermal conductivity coefficient, and even more so the thermal diffusion factor, are difficult to measure accurately, so that fewer data, especially for temperatures other than room temperature, are available for them.

Pressure broadening and shifting of spectral lines also provide bulk data sensitive to features of the repulsive wall of the PES, but only weakly sensitive to its anisotropy. Most such data are not particularly precise (typically with experimental uncertainties of order 5%) and have been obtained for rovibrational transitions.

Bulk relaxation phenomena, such as the relaxation of nuclear spin magnetizations, pressure broadening of the depolarized Rayleigh light scattering spectrum, the effects of magnetic and electric fields on transport properties, and rotational and vibrational relaxation, depend more critically⁴³ upon the anisotropic components of the PES in the sense that they vanish for purely isotropic interactions. Accurate data, especially data providing the temperature dependence of these phenomena, are generally not currently available; such data would be

particularly useful both for delineating between different PESs and for enabling a more accurate determination to be made of the anisotropy of the repulsive wall of the PES. At present the only bulk relaxation data available for Ne–CO mixtures are the state-to-state rotational relaxation rate constants obtained by Hostutler *et al.*²⁵ at temperature 296 K from IR-IR double resonance experiments for CO($v=2$).

A. The interaction second virial coefficient

The temperature dependence of the interaction second virial coefficient, $B_{AB}(T)$, for the Ne–CO interaction ($A \equiv \text{CO}$, $B \equiv \text{Ne}$ hereinafter) has been computed semiclassically, including translational and rotational quantum corrections through first order.⁴⁴

The interaction second virial coefficient, $B_{AB}(T)$, has been calculated for the Ne–CO interaction as a function of temperature over the temperature range $123 \leq T/\text{K} \leq 463$. Table I gives a comparison of the $B_{AB}(T)$ values calculated for the $\text{XC}(\text{fit})_{r=r_e}$, $\overline{\text{XC}(\text{fit})}_{v_{\text{CO}}=0}$, SAPT, and S2 PESs with the reliable (estimated uncertainties $\pm 1 \text{ cm}^{-3} \text{ mol}^{-1}$) experimental data of Brewer²⁶ and with the more recent experimental data of Vatter *et al.*²⁷ The virial coefficients calculated with the two XC PESs lie well within both the $\pm 1 \text{ cm}^{-3} \text{ mol}^{-1}$ uncertainties for the Brewer²⁶ data and the more conservative assigned uncertainties for the Vatter *et al.*²⁷ data. Values of $B_{AB}(T)$ obtained from the SAPT PES by Moszynski *et al.*⁴⁵ and from the S2 PES by McBane and Cybulski¹⁵ are given in columns five and six of Table I, respectively, for comparison with the XC calculations: most values obtained from these two PESs fall on either side of the present calculations, but the values obtained from the S2 PES are in better agreement with the XC values, especially at lower temperatures. Agreement between the Brewer $B_{AB}(T)$ data and the corresponding values calculated from the SAPT PES is poorer

than that for either the XC PESs or the S2 PES.

The ordering of the virial coefficients from the S2, SAPT, and XC(fit) surfaces at higher temperatures can be understood in a straightforward way. The repulsive wall contours shown in Fig. 1 indicate that the S2 repulsive core has a slightly larger volume than that of XC(fit) because of its thicker “waist”, and the XC(fit) attractive well is deeper than the S2 well by about 1 cm^{-1} . Both those differences should make the S2 virial coefficients greater than those from XC(fit), and in fact the computed virial coefficients are greater for the S2 PES for all temperatures above 200 K. Below 200 K the coefficients from the two surfaces are very similar. The virial coefficients computed from the SAPT surface are consistently lower than those from the other two surfaces, and the difference is greater at lower temperatures. That difference is consistent with the roughly 4 cm^{-1} deeper SAPT well.

The level of agreement between these calculations and experiment may be compared in terms of dimensionless root-mean-square deviations (DRMSDs): appropriate DRMSD values have been given in the final row of Table I. The XC and S2 values lie on average well within the experimental uncertainties for the set of eight virial data (i.e., their DRMSD values are less than 1), while the SAPT values fall on average slightly outside the experimental uncertainties. References 28 and 45 give more conservative estimates of experimental uncertainties for the Brewer²⁶ data, namely, $\pm 3 \text{ cm}^{-3} \text{ mol}^{-1}$ for temperatures less than 200 K and $\pm 2 \text{ cm}^{-3} \text{ mol}^{-1}$ for temperatures greater than 200 K. If these uncertainties are employed, all DRMSD values lie well below 1 for all four PESs.

B. Pressure broadening

1. Pure rotational transitions

Nerf and Sonnenberg²¹ reported measurements of the pressure broadening of the $1 \leftarrow 0$ rotational transition at temperatures of 77, 198, and 294 K. More recently, Colmont et al.²² reported pressure broadening measurements on the $3 \leftarrow 2$ transition at 304 K. At 77 K, the average collision energy is comparable to the depth of the Ne–CO attractive well, so that the description of the well has an important effect on predicted cross sections. At the higher temperatures, the size of the repulsive core more strongly affects the pressure broadening cross sections.

McBane and Cybulski¹⁵ computed pressure broadening cross sections for the $1 \leftarrow 0$ transition from the S2 and SAPT PESs and showed that both surfaces predicted values within the experimental error bars of Nerf and Sonnenberg.²¹ New calculations have been carried out for both the $1 \leftarrow 0$ and $3 \leftarrow 2$ rotational transitions for the $\overline{\text{XC}}(\text{fit})_{v_{\text{CO}}=0}$, S2, and SAPT surfaces. Scattering calculations with the accurate CC method were carried out up to 1500 cm^{-1} with the PMP MOLSCAT parallel version of the MOLSCAT program,⁴⁶ and the pressure broadening cross sections were then constructed using the accurate Shafer-Gordon theory⁴⁷ as implemented in a program by Green.⁴⁸ The energy grid for thermal averaging employed spacings of 1 cm^{-1} from 0 to 50 cm^{-1} , 2 cm^{-1} from 50 to 150 cm^{-1} , 10 cm^{-1} from 150 to 400 cm^{-1} , 20 cm^{-1} from 400 to 1200 cm^{-1} , and 100 cm^{-1} from 1200 to 1500 cm^{-1} . These calculations were similar in most respects to those employed in the computation of the integral and differential cross sections described in Section III; at least two closed rotational channels were included and the upper limit on J in the partial wave sum was chosen to

ensure convergence within each energy range. Only the real, diagonal, part of the cross section matrix was employed, because only pressure broadening (not shifting) coefficients of well-isolated lines are considered here. The average Ne atomic mass was used in all calculations. Thermally averaged cross sections were computed according to

$$\sigma_{f \leftarrow i}(T) = \frac{1}{(k_{\text{B}}T)^2} \int_0^{\infty} E \sigma_{f \leftarrow i}(E) e^{-E/(k_{\text{B}}T)} dE, \quad (3)$$

in which E is the collision energy. The integration was carried out by the overlapping-parabolas method.⁴⁹ Thermally averaged cross sections were converted to pressure broadening coefficients in “wavenumber/pressure” form via $\tilde{\gamma} = \bar{c}_{\text{AB}}\sigma(T)/(2\pi ck_{\text{B}}T)$, with k_{B} the Boltzmann constant, $\bar{c}_{\text{AB}} = (8k_{\text{B}}T/(\pi\mu))^{1/2}$ the mean relative thermal speed, μ the Ne–CO reduced mass, and c the speed of light. For ease of comparison all relevant results have been converted to $\tilde{\gamma}$ in units of $\text{cm}^{-1}/\text{atm}$.

The results of these computations using the $\overline{\text{XC}(\text{fit})}_{v_{\text{CO}}=0}$, S2, and SAPT surfaces are shown in Table II. The newly-computed S2 and SAPT values differ modestly from those reported by McBane and Cybulski¹⁵ because close-coupled scattering calculations and a denser energy grid have been employed here.

All three surfaces give results for the $1 \leftarrow 0$ transition well within the experimental uncertainties for all temperatures listed. For the more precise $3 \leftarrow 2$ measurement, the XC(fit) result is lower than the experimental result by slightly more than the reported experimental overall error limit. The SAPT result lies just within that limit, while the S2 result, the largest, lies well within the experimental range.

Elastic collisions that change only the rotational phase or orientation of the CO and inelastic collisions that change j both contribute to pressure broadening. The broadening

coefficients are not particularly sensitive to the anisotropy, since a small change in anisotropy may shift transition probability among different rotational transitions but will not change the total collision rate by very much. Within a hard-shell model, appropriate when $k_B T$ is much larger than the well depth, it is therefore reasonable to expect the pressure broadening coefficients to be related to the total classical cross section σ_{cl} for Ne–CO collisions. The total classical cross section for a convex hard shell may be computed from its surface area S by the Cauchy surface area formula,⁵⁰ $\sigma_{\text{cl}} = S/4$. Using the 150 cm⁻¹ contour to represent the hard shell radius gives $\sigma_{\text{cl}} = 28.25 \text{ \AA}^2$ for the $\text{XC}(\text{fit})_{r=r_e}$ PES, 28.26 \AA^2 for the $\overline{\text{XC}(\text{fit})}_{v_{\text{CO}}=0}$ PES, 28.33 \AA^2 for the SAPT PES, and 28.53 \AA^2 for the S2 PES. The S2 PES has the largest cross section and the $\text{XC}(\text{fit})_{r=r_e}$ PES (similarly, the $\overline{\text{XC}(\text{fit})}_{v_{\text{CO}}=0}$ PES) the smallest, yielding the same relative ordering as the pressure broadening coefficients. The origin of the differences in total classical cross section is apparent in Fig. 1: the $\text{XC}(\text{fit})_{r=r_e}$ PES is narrower at the “waist” near 90° than is the S2 PES, and is narrower near the Ne–C–O linear arrangement than is the SAPT PES.

2. Rovibrational transitions

Experimental data for the Ne pressure broadening of lines in the CO fundamental vibrational band were obtained by Draegert and Williams;²⁴ the broadening for a single additional line, $R(24)$, has been reported at high precision by Henry et al.⁵¹ Corresponding data for lines in the first vibrational overtone band were obtained by Bouanich.²³

While pressure broadening coefficients for rovibrational absorption lines are usually similar to those for the corresponding pure rotational lines, they are not identical. In a rovibrational transition the final state belongs to a different vibrational level and its collision rates, both

elastic and inelastic, may be different. In addition vibrationally inelastic transitions become possible, and they may also contribute to broadening. A straightforward Shafer–Gordon computation of the broadening for infrared lines is very demanding, because the collisional basis set must include levels from multiple vibrational states so that the total energy, and therefore the basis set size, becomes large. Instead, approximations that require scattering calculations only within one vibrational state at a time have been employed here.

The simplest approach is to estimate the broadening coefficients with the assumption that only rotationally inelastic collisions contribute to the broadening. The sum of all rate coefficients out of one rotational level j within a single vibrational state v is represented by

$$k_{vj}^{\text{loss}} = \sum_{j' \neq j} k_{vj' \leftarrow vj}. \quad (4)$$

The broadening coefficient is then given by²⁵

$$\tilde{\gamma}(v'j' \leftarrow v''j'') = \frac{1}{4\pi ck_{\text{B}}T} (k_{v'j'}^{\text{loss}} + k_{v''j''}^{\text{loss}}). \quad (5)$$

The S2 and SAPT PESs are rigid rotor surfaces with no provision for modification in higher vibrational levels; for these surfaces, the same sets of rate coefficients were utilized for both v' and v'' in Eq. (5). Separate sets of rate coefficients were computed for each vibrational level using the XC PESs: for $v = 0$, the $\overline{\text{XC}}(\text{fit})_{v_{\text{CO}}=0}$ PES was employed, while for $v = 1$ and 2, the $\overline{\text{XC}}_{v_{\text{CO}}=1}$ and $\overline{\text{XC}}_{v_{\text{CO}}=2}$ surfaces, as described in Ref. 9, were utilized. These surfaces include the vibrational motion of CO in an average way, but have not been adjusted to match any experimental data describing $v = 1$ or 2. The energy grid and scattering calculations were the same as those described in the previous section, except that an additional set of

coupled states (CS) calculations extending from 1600 to 2500 cm^{-1} in steps of 100 cm^{-1} was added to ensure convergence for higher initial states. The CS results joined smoothly onto the lower-energy CC ones, and they contribute a small fraction of the total rate coefficients even for $j'' \sim 20$, so they should not contribute substantial error.

The resulting pressure broadening coefficients are plotted in Fig. 5 along with the experimental results. No computed result has been plotted for the 1–0 band at $m = 25$ for comparison with the measurement of Henry et al.⁵¹ because the energy grid employed here is inadequate to provide a converged value for that broadening coefficient.

These inelastic-only broadening coefficients ignore both elastic collisions and vibrationally inelastic processes, and should therefore be underestimates. In the Ne–CO system vibrational relaxation should be very slow so the corresponding broadening is probably truly negligible. However, elastic collisions may contribute significant additional broadening. For the rigid-rotor S2 and SAPT surfaces, comparison between the Shafer-Gordon results of Table II and those obtained from Eq. (5) indicates that elastic processes contribute 8–11% to the $R(0)$ ($m = 1$) broadening coefficient and 4–5% to $R(2)$. The elastic contribution can be expected to decline as m increases. For the XC surfaces, adapted for each vibrational level, a better approximation is available. A comparison of the Shafer–Gordon result and Eq. (5) permits an estimate of the broadening due to elastic collisions within each vibrational level. If the elastic contribution is attributed equally to the initial and final levels of the pure rotational transition, then the broadening coefficient for a rovibrational transition becomes approximately

$$\tilde{\gamma}(v'j' \leftarrow v''j'') \approx \frac{1}{4\pi ck_B T} \left(\bar{c}_{AB}[\sigma_B(v''j' \leftarrow v''j'') + \sigma_B(v'j' \leftarrow v'j'')] + \frac{1}{2}(k_{v''j''}^{\text{loss}} - k_{v''j'}^{\text{loss}} + k_{v'j'}^{\text{loss}} - k_{v'j''}^{\text{loss}}) \right) \quad (6)$$

where $\sigma_{\text{B}}(vj' \leftarrow vj'')$ is the real part of the Shafer-Gordon line shape cross section for a pure rotational transition between levels j'' and j' within vibrational level v . Eq. (6) approximates the broadening coefficient for a rovibrational transition as the average of the coefficients for corresponding pure rotational transitions within the two vibrational states involved, plus a correction term that approximately accounts for the different susceptibilities to *elastic* perturbations in the two states. The resulting broadening coefficients for the 2–0 $R(0)$, $R(2)$, and $R(4)$ lines are plotted as open diamonds in Fig. 5. Similar corrections can presumably be expected for the S2 and SAPT surfaces.

When the contribution from elastic collisions is considered, all three surfaces are in generally good agreement with the infrared line broadening data. The S2 PES gives the largest predicted coefficients except for the $R(0)$ line, for which the SAPT PES predicts the highest value. The XC surfaces give the lowest broadening coefficients. The inelastic-only cross sections are slightly too low in the 2–0 band, especially for $m < 10$, but the limited information on elastic contributions suggests that accurate predictions from all surfaces will lie within the experimental error bars. In the 1–0 band, the inelastic-only coefficients agree better with experiment, and for most lines the correction for elastic contributions can be expected to make the agreement slightly worse but still within the error limits.

Overall, the computed pressure broadening coefficients reflect the slightly more compact repulsive core of the XC surfaces clearly, but the differences are small compared to experimental measurement uncertainties. All three surfaces are capable of predicting most pressure broadening observations within experimental error. The single high-precision measurement of Colmont et al.²² does, however, suggest that the XC repulsive core may be slightly too small.

C. Rotational relaxation

Hostutler et al.²⁵ reported time-resolved infrared absorption measurements on CO($v = 2, j'$) following selective excitation of rotational levels j of CO in its $v = 2$ vibrational level in a Ne bath at 296 K. They were unable to extract a unique set of state-to-state rate coefficients from the data, but they fitted their temporal absorption profiles to rate coefficient matrices computed from two empirical fitting laws. They also compared the profiles to predictions using a rate coefficient matrix computed from the S2 PES. They found that the rate coefficient sets from both the “modified exponential gap” (MEG) model and from the S2 PES gave satisfactory agreement with the measurements.

A direct comparison to the experimental data of Hostutler is complicated, and it was decided not to test the XC PES in that fashion. Instead, a rate coefficient matrix has been computed from the $\overline{\text{XC}}_{v_{\text{CO}}=2}$ PES at 296 K and compared to the S2 PES and MEG matrices for $0 \leq j \leq 20$. Throughout that range, for $\Delta j \equiv j' - j'' \leq 3$ the MEG rate coefficient is smaller than the XC and S2 coefficients, and the latter two are closer together than either is to the MEG result. For higher values of Δj , the XC and S2 rate coefficients are very close together and display interference oscillations similar to those in Figures 3 and 4. The MEG coefficients decrease smoothly over the same range without oscillations, so that they are alternately lower and higher than the S2 and XC results. For most values of Δj the XC coefficients lie between the S2 and MEG values; the single exception is for $\Delta j = 2$, for which the XC result is the largest for nearly all j . It is clear from this comparison that the XC rate matrix would provide just as good a fit to the data of Hostutler et al. as does either the S2 rate matrix or the fitted MEG model.

D. Transport Properties.

Full classical trajectory (CT) calculations have been carried out for both the $\text{XC}(\text{fit})_{r=r_e}$ and $\overline{\text{XC}(\text{fit})}_{v_{\text{CO}}=0}$ PESs using the atom-diatom CT code developed by Dickinson and Lee.^{52–54} The generalized effective cross sections required for the description of bulk transport and relaxation phenomena for atom-diatom interactions are calculated as Maxwellian averages over total energy; details regarding the nature⁵⁵ of these cross sections and working expressions for them⁵⁴ are given elsewhere.

Thermal averaging is achieved by employing Chebychev interpolation schemes⁵⁶ in which 7, 11, 7 energy points are employed, respectively, to cover the energy domains $[0.15, 1.50]$, $[1.50, 15.0]$, $[15.0, 300.0]$ in reduced energy units ϵ (given by the absolute minimum energy for the PES for which the calculations are being performed). For the $\text{XC}(\text{fit})_{r=r_e}$ PES, ϵ has the value $225.14 \mu E_h$ (49.41 cm^{-1} , or 69.5 K); ϵ has essentially the same value for the $\overline{\text{XC}(\text{fit})}_{v_{\text{CO}}=0}$ PES.

A 12-point gaussian quadrature has been employed for the integration over the internal energy partition parameter $w = (\epsilon_{\text{rot}} - \epsilon_{\text{trans}})/(\epsilon_{\text{rot}} + \epsilon_{\text{trans}})$. The contribution from the highest value, $w = 0.98516$, can be neglected, as most of the integrands are weighted by $(1 - w)^2$. Integrations over the impact parameter b typically employ 16–20 points, and the calculations are split into integrations over two domains, one above and one below a value of b chosen to be close to the impact parameter value b_r corresponding to the rainbow angle. Finally, the averages over the three relevant angles were carried out using 8–14 gaussian points for each variable. This choice of quadrature points has resulted in the calculation of more than 2.9×10^6 trajectories for the entire calculation for each individual PES. The CT results have been utilized to evaluate the standard expressions for the binary diffusion, binary mixture

shear viscosity, binary mixture thermal conductivity, and binary mixture thermal diffusion factor as given, for example, in Ref. 57, for comparison with experimental results.

Predominantly elastic effective cross sections, such as those governing the binary diffusion and shear viscosity coefficients, have also been calculated using the simple Mason–Monchick (MM) approximation¹⁸ for all four Ne–CO potential energy surfaces so that their usefulness for the calculation/prediction of the temperature dependence of the diffusion coefficient (which, in lowest order, does not depend upon the concentrations of the components) and the interaction viscosity (a quantity that depends only upon the unlike interaction and can be extracted from binary mixture shear viscosity data).

Kinetic theory expressions for the transport coefficients are traditionally represented in terms of a sequence of approximations referred to⁴³ as first, second, \dots , Chapman–Cowling approximations. Although it can be anticipated for Ne–CO mixtures that the second Chapman–Cowling approximation, $[L_{AB}]_2$, for transport coefficient L_{AB} typically differs from the first approximation, $[L_{AB}]_1$, by no more than 3%, second-approximation calculations will be necessary, especially when comparisons of calculated values of transport coefficients are to be made with experimental data having uncertainties smaller than 1%. Second approximations are obtained by multiplying first approximation results by appropriate correction factors, $f_{\text{mix},L}^{[2]}$, that depend upon the mole fraction, X_A , of the molecular species A. Because no full second-approximation correction expressions are currently available for molecule-molecule or atom-molecule mixtures, second approximation corrections for atom-atom mixtures, as defined explicitly elsewhere for binary diffusion,⁵⁸ mixture shear viscosity,⁵⁹ and mixture thermal conductivity,⁶⁰ have been employed. All atom-atom second-approximation correction factors have been obtained by evaluating the required molecular

collision integrals within the MM approximation¹⁸ using the present XC(fit)_{r=r_e} PES for the Ne–CO interaction and relevant literature potentials^{61,62} for the Ne–Ne and CO–CO interactions.

1. *The Binary Diffusion Coefficient.*

The binary diffusion coefficient is given in first Chapman–Cowling approximation by^{43,57}

$$[D_{AB}]_1 = \frac{k_B T}{n \bar{c}_{AB} m_A \mathfrak{S}(1000|A)_{AB}}, \quad (7)$$

in which n is the number density, \bar{c}_{AB} is the mean relative thermal speed, m_A is the mass of the molecule (here CO), and $\mathfrak{S}(1000|A)_{AB}$ is the diffusion (effective) cross section. In this approximation, D_{AB} is determined solely by the unlike interaction between chemical species A and B.

Values for $[D_{AB}]_1$ have been obtained from full CT calculations for the two XC(fit) PESs and the SAPT and S2 PESs. These results are displayed in Table III, together with the reliable Trengove *et al.*²⁸ experimental binary diffusion results obtained using trace amounts of CO in Ne. Mason⁶³ and others^{64,65} have established that when these experimental conditions apply the second approximation correction factor $f_{\text{mix},D}^{[2]}$ is very close to unity, so that first approximation values should approximate the full expression quite well.

The CT values obtained from all four PESs are rather similar, lying within approximately 1% of one another. The values of $[D_{AB}]_1$ obtained using the two XC(fit) PESs are almost indistinguishable (differing from one another typically by only $0.0001 \times 10^{-4} \text{ m}^2\text{s}^{-1}$, or 0.03%), and are in excellent agreement with the Trengove *et al.*²⁸ data, having an average

absolute deviation of only 0.1%, and lying well within the reported uncertainty intervals of $\pm 0.3\%$. The CT values of $[D_{AB}]_1$ obtained using the SAPT and S2 PESs lie on average 0.61% and 0.88%, respectively, below the experimental values, and well outside the reported experimental uncertainty intervals.

The diffusion coefficients from the three surfaces follow the ordering that would be predicted by the total classical cross sections computed from the 150 cm^{-1} repulsive contours described earlier. While one pressure broadening measurement indicated that the XC core was slightly too small and the S2 core better, the opposite conclusion is reached here: the value for the XC diffusion coefficient matches the data very well, while the S2 value is too low, indicating too large a repulsive core. The subtly different dependences of the diffusion and pressure broadening coefficients on the attractive well and on the anisotropy presumably cause this difficulty in interpretation.

Mason–Monchick approximation¹⁸ calculations of the diffusion coefficient have also been carried out for all four PESs in order to test the usefulness of this approximation for the calculation of diffusion coefficients. Although these approximate calculations, like the full CT calculations, give rather similar values for all four PESs, differing by about 1% from one another, they all lie systematically between 6% and 7% below experiment.

If the diffusion coefficient values deduced by Kestin *et al.*²⁹ from their mixture shear viscosity measurements in the temperature range $298\text{ K} \leq T \leq 474\text{ K}$ are compared with values obtained from the CT calculations for the $\text{XC}(\text{fit})_{r=r_e}$ PES, for example, the calculated values appear on average to be about 3.4% high. Note, however, that the value $0.377 \times 10^{-4}\text{ m}^2\text{s}^{-1}$ (uncertainty $\pm 2\%$) for the binary diffusion coefficient at temperature 323.15 K obtained in Ref. 29 based upon analysis of the mixture shear viscosity data lies 3.4% below the more

accurate directly-measured value of $0.3890 \times 10^{-4} \text{ m}^2\text{s}^{-1}$ (uncertainty $\pm 0.3\%$) obtained by Trengove *et al.*²⁸ at 323.0 K: consequently, these two experimental results do not have overlapping uncertainties. If the derived diffusion coefficients reported in Ref. 29 were shifted to agree with the accurate result of Ref. 28 at 323.0 K, while retaining the $\pm 2\%$ uncertainty, they would be brought into close agreement with the CT results obtained for the four Ne–CO PESs considered here.

2. The Interaction and Mixture Shear Viscosity Coefficients.

Unlike the the first Chapman–Cowling approximation for the diffusion coefficient, the first Chapman–Cowling approximation, $[\eta_{\text{mix}}]_1$, for the mixture shear viscosity coefficient depends both upon the unlike interaction between chemical species A and B and upon the like interactions for (pure) A and B. However, it is possible within this approximation to obtain an expression for a quantity, η_{AB} , referred to traditionally as the interaction (shear) viscosity^{43,58} that, like the first Chapman–Cowling approximation to the binary diffusion coefficient, depends solely upon the unlike AB interaction and is independent of the mole fractions of the mixture components. The interaction viscosity is given by^{43,57}

$$\eta_{\text{AB}} = y_{\text{B}}^2 \frac{2k_{\text{B}}T}{\bar{c}_{\text{AB}}[\mathfrak{S}(2000|\text{A})_{\text{AB}} + \mathfrak{S}(\begin{smallmatrix} 2000 \\ 2000 \end{smallmatrix}|\text{A}^{\text{A}})_{\text{AB}}]}, \quad (8)$$

in which y_{A}^2 is a mass fraction given by $y_{\text{A}}^2 = m_{\text{A}}/(m_{\text{A}} + m_{\text{B}})$, and $\mathfrak{S}(2000|\text{A})_{\text{AB}}$, $\mathfrak{S}(\begin{smallmatrix} 2000 \\ 2000 \end{smallmatrix}|\text{A}^{\text{A}})_{\text{AB}}$ are effective cross sections associated with the collisional transport of momentum. Experimental values for η_{AB} can be extracted from mixture shear viscosity data in the same manner employed previously^{6,66} for N₂–Ar and N₂–Kr binary mixtures. However, an uncertainty of

order $\pm 2\%$ is introduced in the extraction process, even though the original experimental data have uncertainties typically less than $\pm 0.5\%$. Moreover, the second Chapman–Cowling approximation correction, which is of the order of $\pm 0.5\%$ for the shear viscosity, is significantly larger than that for the binary diffusion coefficient, and is of the same order of magnitude as the experimental uncertainties.

A comparison between values for the interaction shear viscosity calculated from the SAPT, S2, $\text{XC}(\text{fit})_{r=r_e}$, and $\overline{\text{XC}(\text{fit})}_{v_{\text{CO}}=0}$ PESs and values of η_{AB} extracted from the experimental mixture shear viscosity data of Ref. 29 is given in Table IV. Values of η_{AB} obtained from CT calculations of the effective cross sections using the four PESs are given in the first row of entries associated with each temperature. The CT values obtained for the two $\text{XC}(\text{fit})$ PESs lie systematically below the values extracted from the Kestin *et al.*²⁹ data by no more than 0.4%, well within the estimated $\pm 2\%$ uncertainty typically associated with this derived quantity. Values of η_{AB} obtained from the vibrationally-averaged $\overline{\text{XC}(\text{fit})}_{v_{\text{CO}}=0}$ PES differ typically by less than 0.05% from those obtained using the $\text{XC}(\text{fit})_{r=r_e}$ PES, while values of η_{AB} obtained from CT calculations for the SAPT and S2 PESs lie on average systematically about 0.8% and 1.0% lower than experiment, but still within the estimated experimental uncertainties.

Values of η_{AB} have also been obtained for each of the PESs using MM approximation calculations, in order to examine its usefulness for calculating η_{AB} . The MM values at each temperature, listed directly below the corresponding CT values in Table IV, lie typically about 2% lower than the CT values, and hence generally lie outside the experimental uncertainties.

In order to compare calculated mixture shear viscosities with experimental data having

uncertainties in the range 0.15%–0.5%, it is necessary to introduce three refinements to the first Chapman–Cowling approximation expression given by^{43,57}

$$[\eta_{\text{mix}}]_1 = \frac{k_B T}{\bar{c}_{AB} \Delta_{AB}} \left[X_A \tilde{\mathfrak{S}}(2000|B) - 2X_A X_B \mathfrak{S}(\frac{2000}{2000}|_B^A)_{AB} + X_B \tilde{\mathfrak{S}}(2000|A) \right], \quad (9)$$

in which X_A and X_B mole fractions of CO and Ne, respectively, the symbol $\tilde{\mathfrak{S}}(2000|k)$ denotes a mixture effective cross section given by

$$\tilde{\mathfrak{S}}(2000|k) \equiv \sqrt{2} X_k y_l \mathfrak{S}(2000|k)_{kk} + X_l \mathfrak{S}(2000|k)_{kl}, \quad k, l = A, B (k \neq l), \quad (10)$$

and Δ_{AB} is the expanded determinant

$$\Delta_{AB} \equiv \tilde{\mathfrak{S}}(2000|A) \tilde{\mathfrak{S}}(2000|B) - X_A X_B \mathfrak{S}^2(\frac{2000}{2000}|_B^A)_{AB}. \quad (11)$$

The three refinements, in the order that they are employed in the construction of columns 3–7 of Table V, are: (1) application of second Chapman–Cowling approximation correction factors and, for the pure molecular component A, also a polarization correction factor,⁶⁷ to allow the extraction of values of $\mathfrak{S}(2000|A)_{AA}$ and $\mathfrak{S}(2000|B)_{BB}$ appropriate to first Chapman–Cowling values for the end-points $[\eta_A^{\text{iso}}]_1$ and $[\eta_B]_1$;^{68,69} (2) calculation of $[\eta_{\text{mix}}]_2$ values from computed $[\eta_{\text{mix}}]_1$ values using a second Chapman–Cowling correction factor $f_{\text{mix},\eta}^{[2]}$, via

$$[\eta_{\text{mix}}]_2 = [\eta_{\text{mix}}]_1 f_{\text{mix},\eta}^{[2]};$$

(3) employment of polarization correction⁶⁷ factors, $f_{02,\eta}$, to give final calculated values,

$\eta_{\text{mix}}^{\text{calc}}$, for comparison with experiment. Numerical values for the $f_{\text{mix},\eta}^{[2]}$ have been obtained as explained more generally prior to subsection IV.C.1. Polarization corrections for both the mixture and pure molecular gas data are typically of order 0.1%–0.3%.

Table V presents values for the mixture shear viscosity calculated in first and second Chapman–Cowling approximations using full CT computations of the relevant effective cross sections for the $\text{XC}(\text{fit})_{r=r_e}$, S2, and SAPT PESs, and of η_{mix} , including the polarization correction.⁴³ Because the $\overline{\text{XC}(\text{fit})}_{v_{\text{CO}}=0}$ PES gives values for η_{mix} that are essentially indistinguishable from those obtained using the $\text{XC}(\text{fit})_{r=r_e}$ PES, they have not been reported in this table. Values for the relevant polarization correction factor,⁶⁷ $f_{02\eta}$, for the mixture shear viscosity are also listed in Table V. Because values of the correction factors $f_{\text{mix},\eta}^{[2]}$ and $f_{02\eta}$ differ by less than 0.05% amongst the four PESs being considered, only the value obtained from the $\text{XC}(\text{fit})_{r=r_e}$ PES has been given for each mixture mole-fraction entry in Table V.

As can be seen from Table V all four PESs give values of η_{mix} that are on the whole in excellent agreement with the experimental results of Ref. 29, with both the S2 and SAPT PESs giving values for η_{mix} that lie well within the experimental uncertainties of $\pm 0.5\%$ assigned to the direct mixture shear viscosity data of Ref. 29. The contribution to η_{mix} of the Chapman–Cowling correction factors for the mixture shear viscosity are about 0.5%, and are the same magnitude as the experimental uncertainties. Surprisingly, the $\text{XC}(\text{fit})_{r=r_e}$ PES, which gives CT values for D_{AB} that agree extremely well with the accurate diffusion data of Ref. 28, gives η_{mix} values that compare more poorly (though still largely within the experimental uncertainties) than do the SAPT and S2 values with the experimental mixture shear viscosity data. The averages of the magnitudes of the differences between the calculated and experimental values are about 0.37%, 0.12%, and 0.10%, respectively, for the

XC, S2, and SAPT PESs; the XC discrepancy is larger than the experimental uncertainty only for $T = 298$ K and $X_A = 0.3715$, in which case it is 0.64%.

3. The Mixture Thermal Conductivity Coefficient

The first Chapman–Cowling approximation, $[\lambda_{\text{mix}}]_1$, to the thermal conductivity for a binary mixture of a diatomic or polyatomic gas with a noble gas is given in the total-energy-flux representation by⁵⁷

$$[\lambda_{\text{mix}}]_1 = \frac{k_B T}{m_A \bar{c}_{AB} \Delta'_{AB}} \left\{ X_A C_P^A \tilde{\mathfrak{S}}(1010|B) - \frac{2y_A}{y_B} \sqrt{\frac{5k_B T C_P^A}{2}} X_A X_B \mathfrak{S}(\overset{10E}{1010} | \overset{A}{B})_{AB} + X_B \frac{5k_B y_A^2}{2y_B^2} \tilde{\mathfrak{S}}(10E|A) \right\}, \quad (12)$$

with k_B , y_A , y_B , \bar{c}_{AB} , X_A , X_B as defined earlier, C_P^A the heat capacity at constant pressure per molecule A, and Δ'_{AB} the expanded determinant

$$\Delta'_{AB} \equiv \tilde{\mathfrak{S}}(10E|A) \tilde{\mathfrak{S}}(1010|B) - X_A X_B \mathfrak{S}^2(\overset{10E}{1010} | \overset{A}{B})_{AB}, \quad (13)$$

in which the quantities $\tilde{\mathfrak{S}}(1010|B)$, $\tilde{\mathfrak{S}}(10E|A)$, and $\mathfrak{S}(\overset{10E}{1010} | \overset{A}{B})_{AB}$ are mixture effective cross sections associated with the collisional transport of energy.^{43,57} Values of $[\lambda_{\text{mix}}]_1$ calculated for the Ne–CO experimental mixture compositions reported in Table VI have been evaluated using Eq. (12) and CT values of the effective cross sections obtained using the SAPT, S2, and the two XC(fit) PESs. Mixture thermal conductivity values have not been reported in Table VI for the $\overline{\text{XC(fit)}}_{v_{\text{CO}}=0}$ PES, as they are essentially indistinguishable from those obtained for the $\text{XC(fit)}_{r=r_e}$ PES.

The only experimental determination of the mixture thermal conductivity for Ne–CO binary mixtures is that of Imaishi and Kestin³⁰ at a temperature of 300.65 K for three different mixture compositions and the pure components. Because the experimental data have uncertainties of only $\pm 0.3\%$, it is necessary, as for the mixture shear viscosity, to include both second Chapman–Cowling approximation and polarization correction factors in order to compare calculated and experimental results. First-approximation values obtained for the mixture thermal conductivity have been converted into second-approximation values via multiplication by Chapman–Cowling correction factors, $f_{\text{mix},\lambda}^{[2]}$, calculated for the translational component of the thermal conductivity within the MM approximation.⁶⁰ Values of $\lambda_{\text{mix}}^{\text{calc}}$ have been obtained from $\lambda_{\text{mix}}^{\text{calc}} = [\lambda_{\text{mix}}]_2 f_{12\lambda}$, in which $f_{12\lambda}$ is the polarization correction factor⁶⁷ appropriate to the thermal conductivity. The correction factors $f_{\text{mix},\lambda}^{[2]}$ and $f_{12\lambda}$ for the thermal conductivity coefficient are, in general, slightly larger than the corresponding correction factors $f_{\text{mix},\eta}^{[2]}$ and $f_{02\eta}$ for the shear viscosity coefficient, and are larger than or comparable to the experimental uncertainty of $\pm 0.3\%$. As for the mixture shear viscosity, it is also important to provide good estimates of second Chapman–Cowling approximation corrections to both pure gas thermal conductivities in order to determine pure gas end-points properly.

From Table VI it can be seen that the level of agreement between the values of $\lambda_{\text{mix}}^{\text{calc}}$ obtained from the present XC(fit) PESs and the experimental mixture thermal conductivity values given by Imaishi and Kestin³⁰ is very good, with deviations from experiment lying on average at the specified experimental uncertainties of $\pm 0.3\%$. The values of $\lambda_{\text{mix}}^{\text{calc}}$ obtained from the S2 PES give slightly better agreement with experiment, with absolute deviations averaging 0.21%, while the SAPT PES does not give as good agreement with experiment,

with deviations averaging more than double the experimental uncertainty.

4. *The Thermal Diffusion Factor*

Although expressions describing thermal diffusion in binary mixtures of noble gases have been available for many years, having appeared in the first edition (1939) of the classic monograph by Chapman and Cowling,⁷⁰ it wasn't until recently that reliable appropriate expressions have become available⁷¹ for mixtures containing molecules. Utilization of the formulae given in Ref. 71 for the two-flux expression for the thermal diffusion factor α_T , together with reliable CT values for the set of relevant effective cross sections, showed good agreement with experiment for a number of atom-molecule binary mixtures.^{68,69,72-74} Indeed, a significant difference between the values for α_T calculated using the monatomic mixture formula^{43,70} and the full thermal diffusion factor formula of Ref. 71 was found for Ne-N₂ mixtures;⁷² this suggests that similar additional contributions may also exist for binary mixtures of Ne with the isoelectronic CO molecule.

The thermal diffusion factor can be split formally into two parts as

$$\alpha_T = \alpha_T^{\text{iso}} + \alpha_T^{\text{pol}}, \quad (14)$$

in which α_T^{iso} is the component of the thermal diffusion factor that corresponds to an isotropic nonequilibrium distribution function⁴³ and α_T^{pol} , referred to as the polarization contribution, is associated with the dependence of the nonequilibrium distribution function upon the vectorial nature of the molecular angular momentum. The polarization contribution is, however, often only a small fraction of α_T .

As shown in Ref. 71, there are two distinct, yet similar, approximations for α_T , referred to as the two-flux and total-energy-flux approximations. The form taken by α_T^{iso} , in particular, differs for these two approximations. For the two-flux approximation, α_T^{iso} can be written as

$$\alpha_T^{\text{iso}}(2\text{F}) \equiv \alpha_T^{\text{mon}}(2\text{F}) + \alpha_T^{\text{int}} + \alpha_T^{\text{cf}}, \quad (15)$$

in which $\alpha_T^{\text{mon}}(2\text{F})$ reduces to the expression for the thermal diffusion factor for a binary monatomic gas mixture when both mixture constituents are atoms, α_T^{int} represents the contribution to α_T^{iso} from the internal (vibrational and/or rotational) energy in the absence of translational-internal energy coupling, and α_T^{cf} represents the contribution to α_T^{iso} due to collisional coupling of the translational and internal energy fluxes. For the total-energy-flux approximation, α_T^{iso} can be written as

$$\alpha_T^{\text{iso}}(\text{totE}) \equiv \alpha_T^{\text{mon}}(\text{totE}) + \alpha_T^{\text{mol}}, \quad (16)$$

in which $\alpha_T^{\text{mon}}(\text{totE})$ reduces to the thermal diffusion factor for a binary monatomic mixture when both mixture constituents are atoms, and α_T^{mol} represents the additional contributions to α_T^{iso} present only for molecular constituents.

Calculations of the thermal diffusion factor α_T based upon the two-flux and total-energy-flux approximations,⁷¹ and employing CT values for the relevant effective cross sections obtained from the $\text{XC}(\text{fit})_{r=r_e}$, $\overline{\text{XC}(\text{fit})}_{v_{\text{CO}}=0}$, SAPT, and S2 PESs are compared with experiment in Table VII. The experimental data are sparse, being available only at temperature $T = 300$ K and only for four values of the mole fraction, X_{CO} , of CO. Further, the mole fraction values appear in the form of two pairs, with the two values for each pair sufficiently near

that the differences in the two experimental values of α_T are comparable to the experimental uncertainty of $\pm 3.5\%$. Comparison between theory and experiment is further complicated by the two approximations yielding significantly different values for α_T for a given PES. As an aid to the discussion that follows, the relative behavior of the four PESs in predicting the experimental thermal diffusion results for Ne–CO mixtures for both approximations are presented in Table VIII, which also contains the related relative results for $\alpha_T(\text{totE})$ versus $\alpha_T(2F)$.

For each PES considered here the results for the 2F approximation are always higher than those obtained from the totE approximation; the difference between results obtained with the two approximations decreases ‘significantly’ as the mole fraction increases from $X_{\text{CO}} = 0.185, 0.200$ to $X_{\text{CO}} = 0.785, 0.815$. From the first row of Table VIII, it can be seen that the differences are remarkably consistent from one PES to another. Moreover, in all cases the $\alpha_T(2F)$ results lie closer to experiment than do the $\alpha_T(\text{totE})$ values, particularly for the smaller mole fractions. The absolute average deviations (AAD) between the calculated values of α_T and experiment for each of the four PESs and for both approximations are provided in Table VIII. In the following, however, consideration will be limited to the calculated results for α_T obtained from the apparently more reliable two-flux approximation.

As might be expected from the comparisons already made for the other transport properties, the results obtained from the two XC(fit) PESs are very similar, and differ uniformly by about 0.5% for each value of X_{CO} . The two-flux results agree (essentially) with experiment to within the experimental uncertainty only for the two lowest mole fractions. The two-flux results for the S2 and SAPT PESs are similar as functions of X_{CO} , and also agree with experiment only for the two smallest mole fractions; however, that agreement is considerably

better than is seen for the XC PESs.

Prior to the publication of a detailed expression for the thermal diffusion factor for binary mixtures involving molecules in 2003,⁷¹ the only expression for the thermal diffusion factor was that obtained for noble gas binary mixtures by Chapman⁷⁵ in 1917 (see also Ref. 70). The monatomic formula has routinely been employed for the calculation of α_T for atom-molecule mixtures and even for purely molecular mixtures: it was the use of this formula coupled with inaccurate collisional approximations that was the source of significant disagreements between theory and experiment.⁷⁶⁻⁷⁹

The quantities α_T^{mon} appearing in each of Eqs. (12) and (13) correspond to the monatomic Chapman expression for α_T . An examination of the explicit expressions given for them in Ref. 71 shows that while the two expressions are distinct and different, they both reduce to the classic Chapman expression in the limit of binary monatomic mixtures. The two-flux expression for $\alpha_T^{\text{mon}}(2F)$, because it is based upon the contribution to thermal diffusion from the translational heat flux, has a 1–1 correspondence with the effective cross section combinations that occur in the Chapman expression and contains almost no contributions associated with the internal states of the molecular component. The total-energy-flux expression, $\alpha_T^{\text{mon}}(\text{totE})$, has the same structure as the monatomic Chapman expression for α_T , but it inherently includes much of the molecular internal state contributions to thermal diffusion via the detailed structures of the effective cross sections.

As can be seen from Table VII, the values for $\alpha_T^{\text{mon}}(2F)$ overestimate the full $\alpha_T(2F)$ by about 50% on average both for $X_{\text{CO}} \leq 0.2$ and $X_{\text{CO}} \geq 0.785$, while those for $\alpha_T^{\text{mon}}(\text{totE})$ underestimate the full $\alpha_T(\text{totE})$ by about 6.5% on average for $X_{\text{CO}} \leq 0.2$ and by about 4.5% for $X_{\text{CO}} \geq 0.785$. Notice, however, that once the internal energy flux contribution has been

included in the two-flux approximation to give $\alpha_T^{\text{iso}}(2\text{F})$, the full $\alpha_T(2\text{F})$ is underestimated, on average, by about 5% for $X_{\text{CO}} \leq 0.2$ and by about 2.6% for $X_{\text{CO}} \geq 0.785$. At this level of theory these two-flux results are more comparable with those for the total-energy-flux approximation for α_T^{iso} , which underestimates $\alpha_T(\text{totE})$ by about 7.6% and 4.6% respectively. The full theoretical results for α_T , which were discussed and compared with experiment in the context of Table VIII, also include the corresponding polarization contributions to the thermal diffusion factor.

V. GENERAL DISCUSSION.

Based upon the analysis presented in Sections III and IV, and elsewhere⁹ for the MW, MMW, and mid-IR spectroscopic transition frequencies for various isotopologues of Ne–CO, the two XC(fit) PESs offer the best representation of the Ne–CO interaction currently available. Because the results obtained for the beam scattering and bulk gas mixture properties being considered here are indistinguishable for the two XC(fit) PESs, they will be referred to collectively as the XC(fit) PES. It is clear from the results obtained in Ref. 9 that the XC(fit) PESs provide a far superior representation of the Ne–CO interaction for the calculation of spectroscopic transition frequencies than does the original SAPT PES or the S2 PES; they are superior even to a version¹⁴ of the SAPT PES that was scaled to improve agreement with experimental mid-IR spectral results. However, the performance of the XC(fit) PES relative to the SAPT and S2 PESs with regard to the beam scattering and bulk gas mixture properties being considered explicitly here requires a more detailed discussion.

The ability of the potential energy surfaces considered in this paper to reproduce the experimental results for the various properties of Ne–CO mixtures discussed in Sections III

and IV are summarized in Table IX. This table and discussion related to it apply to results obtained at the highest level of theory (i.e. close-coupled scattering calculations of the microscopic properties, and CT calculations of transport properties). As pointed out in Section IV.C.4, the discussion of the calculated results for the thermal diffusion factor is complicated by the sparseness of reliable experimental data and differences between the calculated results obtained from two relatively recent⁷¹ approximations for this property; the entries in Table IX are based upon results obtained from employing the two-flux approximation for α_T . The comparison between calculated and experimental results for the state-to-state differential cross sections and the state-to-state relative product densities (which are related to the corresponding integral cross sections) of Section III is more qualitative in nature, with a focus on agreement with experiment in the trends of observables as a function of scattering angle and/or final rotational state.

It will be clear from Table IX and related discussions in Secs. III and IV that the XC(fit) and S2 PESs give the best representations of the Ne–CO interaction as sensed by the combined bulk properties/beam scattering data. Based primarily upon the difference between results obtained for the two PESs for the binary diffusion coefficient, the XC(fit) PES gives a marginally better representation than does the S2 PES; for all other properties surveyed in Table IX, the XC(fit) and S2 PESs give comparably good agreement with experiment, in each case giving calculated results that lie essentially within the experimental uncertainties. The SAPT PES also gives very good results for many of the properties considered in Table IX, but does not agree with experiment for binary diffusion, mixture thermal conductivity, interaction second virial coefficient, and the beam scattering data. The interaction second virial coefficient data depend upon both the repulsive core and the attractive well of the PES,

while the diffusion coefficient and mixture interaction shear viscosity are dominated by the behavior of the repulsive core. The deeper well of the SAPT PES is largely responsible for its disagreement with the virial coefficient data and its slightly greater anisotropy is likely the source of its disagreements with the scattering data. Indeed, the relative ordering of the XC, S2, and SAPT surfaces found in Table I (interaction second virial coefficient) is consistent with the combination of hard-shell cross sections and well depths of the three surfaces, while the comparisons in Tables II (diffusion coefficient) and III (interaction mixture viscosity) are consistent with the ordering of the hard-shell cross sections for the three surfaces. As the mixture thermal conductivity [see Eqs.(12) and (13)] is a subtle blend of hard-sphere and anisotropy contributions, it is more difficult to visualize its relative behavior, but the ordering of the three surfaces seen in Table VI is indeed consistent with the ordering of the strengths of the anisotropies of the three PESs.

It should be emphasized that both the SAPT and S2 PESs are *ab initio* surfaces. For the properties considered in Table IX the quality of agreement between calculations with the S2 PES and experiment is remarkably good; the Ne–CO dimer involves two sizable species and a very subtle interaction, and provides a severe test for *ab initio* techniques. While the SAPT PES does not fare as well in the comparisons presented here, its description of the shape of the Ne–CO well, and its consequent agreement with the spectroscopic data, are superior to those of the S2 PES.

The XC(fit) PES is based upon the exchange-Coulomb potential energy model, which utilizes often readily available or obtainable input, namely long range multipolar interaction energy coefficients and Heitler–London interaction energies (which require isolated species wave functions only; the SCF level of approximation appears to suffice). The flexibility

in the model is crucial to its success, and is provided for the mostly repulsive part of the model by adjustable parameters in the simple function multiplying $E_{\text{HL}}^{(1)}$ and for the mostly attractive part through variations in the long range interaction energy coefficients within their uncertainties. The need for such flexibility is clearly related to the approximations inherent in the construction of the model. The nature and importance of this flexibility, and its balance between the repulsive and attractive parts of the potential energy model, has been discussed in detail elsewhere.^{1-6,66,80,81}

The adjustable parameters in the XC(fit) PES for Ne-CO are determined by fitting to relatively small set of pure rotational transition frequencies that sense features of the potential well in the energy range associated with the rotational levels being excited by the radiation. Nevertheless, the resulting PES reliably predicts a range of spectroscopic transitions, beam scattering cross sections, and bulk properties of the dimer that sample a wide range of configuration space for this interaction that is not well sampled by the spectral data. Similar observations have been made for interactions for which second virial coefficient and/or MW data have been utilized to determine the adjustable parameters in the XC(fit) potential energy model.^{4,5,7,61,66,68,80,82,83}

The XC(fit) PES provides overall the most reliable representation of the Ne-CO interaction to date. This PES also provides a suitable starting point for future studies of this interaction: should new, accurate, data become available for bulk relaxation phenomena, for example, it should be possible to use them to refine the anisotropy of the repulsive wall of the PES. The flexibility still inherent in the XC potential energy surfaces can be exploited, as required, for such a purpose.

Acknowledgments

W.J.M. and F.R.W.M. are grateful to NSERC of Canada for the award of Discovery Grants that have funded this research in part.

TABLE I: Temperature dependence of the interaction second virial coefficient, B_{AB} , for Ne-CO mixtures

T /K	Expt. ^a /cm ³ mol ⁻¹	Calculated values: /cm ³ mol ⁻¹			
		$\overline{XC(\text{fit})}_{r=r_e}$	$\overline{XC(\text{fit})}_{v_{CO}=0}$	SAPT ¹⁴	S2 ¹⁵
123.15	-14.71 ± 1	-14.21	-14.44	-17.26	-14.48
148.15	-5.64 ± 1	-5.12	-5.30	-7.50	-5.28
173.15	0.42 ± 1	0.97	0.83	-0.96	0.90
223.15	7.83 ± 1	8.53	8.43	7.15	8.57
273.15	12.23 ± 1	12.94	12.86	11.88	13.04
296.15	14.1 ± 1.5	14.38	14.31	13.43	14.51
353.15	17.2 ± 2.0	16.99	16.93	16.24	17.15
463.15	20.6 ± 3.0	19.84	19.81	19.34	20.05
DRMSD Value		0.45	0.35	1.3	0.46

^aThe first five experimental values are from Ref. 26; the final three values are from Ref. 27.

TABLE II: Measured and computed pressure broadening coefficients for pure rotational transitions. All coefficients are given in units of $10^{-3} \text{ cm}^{-1}/\text{atm}$. Experimental data are from Ref. 21 for the $1 \leftarrow 0$ line and from Ref. 22 for the $3 \leftarrow 2$ line.

Line	$1 \leftarrow 0$			$3 \leftarrow 2$
	77	198	294	304
Experiment	122 ± 13	60.0 ± 7.1	40.6 ± 4.8	38.4 ± 1.2
$\overline{\text{XC}}(\text{fit})_{v_{\text{CO}}=0}$	120	55.9	41.8	36.9
S2	124	57.8	43.1	37.9
SAPT	123	57.1	42.6	37.3

TABLE III: Comparison of calculated and experimental values for the binary diffusion coefficient of Ne–CO mixtures. The first row associated with each temperature gives the CT values for the diffusion coefficient; the second row gives the corresponding MM value.

T / K	$[D_{AB}]_1 / 10^{-4} \text{m}^2 \text{s}^{-1}$				$D_{AB} / 10^{-4} \text{m}^2 \text{s}^{-1}$
	SAPT	S2	$\text{XC}(\text{fit})_{r=r_e}$	$\overline{\text{XC}(\text{fit})}_{v_{\text{CO}}=0}$	
277.0	0.2988	0.2981	0.3008	0.3009	0.3009
	0.2790	0.2799	0.2820	0.2818	
290.0	0.3230	0.3221	0.3250	0.3251	0.3252
	0.3024	0.3029	0.3052	0.3050	
300.0	0.3420	0.3411	0.3441	0.3442	0.3446
	0.3202	0.3211	0.3235	0.3233	
310.0	0.3615	0.3605	0.3637	0.3638	0.3635
	0.3388	0.3397	0.3423	0.3420	
323.0	0.3874	0.3863	0.3897	0.3898	0.3890
	0.3636	0.3645	0.3672	0.3670	

TABLE IV: Comparison of calculated and experimental interaction shear viscosity values for Ne–CO binary mixtures. The upper row at each temperature gives CT values while the lower row gives MM approximation values for η_{AB} . The final column gives values of η_{AB} extracted from the η_{mix} data of Ref. 29.

T /K	η_{AB} / μ Pa s				
	SAPT	S2	XC(fit) $_{r=r_e}$	$\overline{\text{XC(fit)}}_{v_{\text{CO}}=0}$	Expt.
298.15	23.37	23.27	23.51	23.51	23.53
	22.68	22.71	22.90	22.89	
323.15	24.69	24.58	24.83	24.83	24.88
	24.02	24.02	24.23	24.21	
373.15	27.20	27.08	27.33	27.33	27.41
	26.52	26.51	26.75	26.73	
423.15	29.58	29.45	29.73	29.73	29.84
	28.90	28.88	29.12	29.12	
473.15	31.86	31.72	32.01	32.01	32.13
	31.17	31.15	31.40	31.40	

TABLE V: Comparison between calculated and experimental values of the mixture shear viscosity η_{mix} (units $\mu\text{Pa s}$). The first row associated with each (T, X_{CO}) pair contains results obtained using the $\text{XC}(\text{fit})_{r=r_e}$ PES, the second row contains results obtained using the S2 PES, and the third row contains results obtained using the SAPT PES. δ is given by $100(\eta_{\text{mix}}^{\text{calc}} - \eta_{\text{mix}}^{\text{expt}})/\eta_{\text{mix}}^{\text{expt}}$.

T / K	X_{CO}	Calculated Mixture Shear Viscosity				Expt. ²⁹		
		$[\eta_{\text{mix}}]_1$	$f_{\text{mix},\eta}^{[2]}$	$[\eta_{\text{mix}}]_2$	$f_{02\eta}$	$\eta_{\text{mix}}^{\text{calc}}$	$\eta_{\text{mix}}^{\text{expt.}}$	$\delta / \%$
298.15	0.3715	25.08	1.0051	25.21	1.0020	25.26	25.10	0.64
		24.95		25.08		25.13		0.12
		25.00		25.13		25.18		0.32
	0.6658	21.18	1.0043	21.28	1.0027	21.34	21.24	0.47
		21.09		21.18		21.24		0.0
		21.13		21.22		21.28		0.19
323.15	0.3715	26.52	1.0055	26.66	1.0019	26.71	26.62	0.34
		26.38		26.53		26.58		-0.15
		26.44		26.59		26.64		0.08
	0.6658	22.46	1.0046	22.56	1.0027	22.62	22.54	0.36
		22.36		22.46		22.52		-0.09
		22.40		22.50		22.56		0.09
373.15	0.3715	29.27	1.0057	29.43	1.0019	29.49	29.40	0.31
		29.12		29.29		29.35		-0.17
		29.18		29.35		29.40		0.0
	0.6658	24.89	1.0050	25.02	1.0027	25.09	24.98	0.44
		24.78		24.90		24.97		-0.04
		24.83		24.95		25.02		0.17
423.15	0.3715	31.86	1.0059	32.05	1.0018	32.11	32.04	0.21
		31.71		31.89		31.95		-0.28
		31.77		31.96		32.02		-0.06
	0.6658	27.16	1.0053	27.30	1.0026	27.37	27.28	0.33
		27.04		27.19		27.26		-0.07
		27.09		27.23		27.31		0.11
473.15	0.3715	34.33	1.0061	34.54	1.0019	34.61	34.51	0.29

TABLE VI: Comparison between calculated and experimental mixture thermal conductivities for Ne–CO mixtures at $T = 300.65$ K. (Units: $\text{mW m}^{-1}\text{K}^{-1}$)

X_{CO}	PES	Calculated Mixture Thermal Conductivity					Expt. ³⁰	δ
		$[\lambda_{\text{mix}}]_1$	$f_{\text{mix},\lambda}^{[2]}$	$[\lambda_{\text{mix}}]_2$	$f_{12\lambda}$	$\lambda_{\text{mix}}^{\text{calc}}$	$\lambda_{\text{mix}}^{\text{expt}}$	/%
0.7364	$\text{XC}(\text{fit})_{r=r_e}$	28.86	1.0057	29.08	1.0031	29.17	29.13	0.14
	S2	28.88		29.05		29.14		0.03
	SAPT	28.78		28.94		29.03		-0.34
0.4835	$\text{XC}(\text{fit})_{r=r_e}$	33.99	1.0070	34.23	1.0010	34.27	34.43	-0.46
	S2	34.03		34.27		34.30		-0.38
	SAPT	33.85		34.08		34.12		-0.90
0.2742	$\text{XC}(\text{fit})_{r=r_e}$	39.43	1.0080	39.74	1.0002	39.75	39.88	-0.33
	S2	39.47		39.78		39.79		-0.23
	SAPT	39.28		39.59		39.60		-0.70

TABLE VII: Thermal diffusion factor for Ne–CO mixtures at temperature $T = 300$ K.

X_{CO}	PES	$\alpha_{\text{T}}^{\text{mon}}(2\text{F})$	$\alpha_{\text{T}}^{\text{iso}}(2\text{F})$	$\alpha_{\text{T}}(2\text{F})$	$\alpha_{\text{T}}^{\text{expt}}$	$\alpha_{\text{T}}(\text{totE})$	$\alpha_{\text{T}}^{\text{iso}}(\text{totE})$	$\alpha_{\text{T}}^{\text{mon}}(\text{totE})$
0.185	$\text{XC}(\text{fit})_{r=r_e}$	0.1299	0.0819	0.0864	0.0896	0.0825	0.0760	0.0768
	$\overline{\text{XC}(\text{fit})}_{v_{\text{CO}}=0}$	0.1303	0.0823	0.0868		0.0829	0.0764	0.0772
	S2	0.1312	0.0848	0.0889		0.0847	0.0788	0.0798
	SAPT	0.1300	0.0846	0.0894		0.0855	0.0786	0.0794
0.200	$\text{XC}(\text{fit})_{r=r_e}$	0.1285	0.0812	0.0856	0.0873	0.0817	0.0754	0.0761
	$\overline{\text{XC}(\text{fit})}_{v_{\text{CO}}=0}$	0.1288	0.0816	0.0860		0.0821	0.0758	0.0765
	S2	0.1298	0.0840	0.0880		0.0838	0.0781	0.0790
	SAPT	0.1285	0.0838	0.0885		0.0846	0.0779	0.0786
0.785	$\text{XC}(\text{fit})_{r=r_e}$	0.0902	0.0580	0.0596	0.0659	0.0590	0.0562	0.0562
	$\overline{\text{XC}(\text{fit})}_{v_{\text{CO}}=0}$	0.0903	0.0583	0.0599		0.0593	0.0565	0.0565
	S2	0.0903	0.0592	0.0606		0.0599	0.0574	0.0574
	SAPT	0.0891	0.0586	0.0603		0.0598	0.0568	0.0568
0.815	$\text{XC}(\text{fit})_{r=r_e}$	0.0888	0.0570	0.0585	0.0633	0.0582	0.0555	0.0554
	$\overline{\text{XC}(\text{fit})}_{v_{\text{CO}}=0}$	0.0889	0.0573	0.0588		0.0585	0.0558	0.0557
	S2	0.0889	0.0581	0.0595		0.0590	0.0566	0.0566
	SAPT	0.0877	0.0576	0.0592		0.0589	0.0561	0.0560

TABLE VIII: Relative Behaviors of the Four PESs in Predicting Thermal Diffusion, including the absolute average deviations (AAD) between calculated and experimental results.

Quantity	X_{CO}	Potential Energy Surface			
		$\text{XC}(\text{fit})_{r=r_e}$	$\overline{\text{XC}(\text{fit})}_{v_{\text{CO}}=0}$	S2	SAPT
$\frac{\alpha_{\text{T}}(2\text{F}) - \alpha_{\text{T}}(\text{totE})}{\alpha_{\text{T}}(2\text{F})} \times 100\%$	0.185	4.5%	4.5%	4.8%	4.4%
	0.200	4.5%	4.5%	4.8%	4.4%
	0.785	1.0%	1.0%	1.2%	0.83%
	0.815	0.51%	0.51%	0.84%	0.51%
$\frac{\alpha_{\text{T}}(\text{expt}) - \alpha_{\text{T}}(2\text{F})}{\alpha_{\text{T}}(\text{expt})} \times 100\%$	0.185	3.6%	3.1%	0.78%	0.22%
	0.200	1.9%	1.5%	0.80%	-1.4%
	0.785	9.6%	9.1%	8.0%	8.5%
	0.815	7.6%	7.1%	6.0%	6.5%
$\frac{\alpha_{\text{T}}(\text{expt}) - \alpha_{\text{T}}(\text{totE})}{\alpha_{\text{T}}(\text{expt})} \times 100\%$	0.185	7.9%	7.5%	5.5%	4.6%
	0.200	6.4%	6.0%	4.0%	3.1%
	0.785	10.5%	10.0%	9.1%	9.3%
	0.815	8.1%	7.6%	6.8%	7.0%
AAD _{2F} ($X_{\text{CO}} \leq 0.200$)		2.7%	2.3%	0.8%	0.8%
AAD _{2F} ($X_{\text{CO}} \geq 0.785$)		8.6%	8.1%	7.0%	7.5%
AAD _{totE} ($X_{\text{CO}} \leq 0.200$)		7.1%	6.7%	4.7%	3.8%
AAD _{totE} ($X_{\text{CO}} \geq 0.785$)		9.3%	8.8%	7.9%	8.1%

TABLE IX: A summary of the predictive abilities of various Ne–CO PESs; see Secs. III and IV for details.

Properties	Table	Reference	Uncertainty	XC	S2	SAPT
Virials	I	26	$\pm 1 \text{ cm}^3\text{mol}^{-1}$	easily	easily	no
		27	$\pm 1.5\text{--}3.0 \text{ cm}^3\text{mol}^{-1}$	easily	easily	easily
MW Pressure broadening	II	21	$\pm 10\%$	easily	easily	easily
MMW Pressure broadening	II	22	$\pm 3\%$	close ^a	easily	yes
Diffusion	III	28	$\pm 0.3\%$	easily	no	no
		29	$\pm 2\%$	easily	easily	easily
Interaction Viscosity	IV	29	$\pm 2\%$	easily	yes	easily
Mixture viscosity	V	29	$\pm 0.5\%$	essentially ^b	easily	easily
Thermal Conductivity	VI	30	$\pm 0.3\%$	close ^c	close ^c	no
Thermal Diffusion	VII	28	$\pm 3.5\%$	partially ^d	partially ^d	partially ^d
	Figure					
IR Pressure broadening	5	23,24	$\pm 5\%$	yes	yes	yes
State-to-state differential cross sections	2	20		yes	yes	no ^e
State-to-state relative product densities and integral cross sections	3, 4	19		partially ^f	partially ^f	no ^g
Rotational relaxation rates ^h		25		easily	easily	

^aXC disagrees with the single measurement by 1.3 times its overall uncertainty.

^bThere are ten data points. The prediction for $T = 298.15 \text{ K}$, $X_{\text{CO}} = 0.3715$ is 0.64% higher than experiment.

^cThere are three data points. The S2 result is lower than experiment by 0.37% at $X_{\text{CO}} = 0.4835$, while the XC results are low by 0.48% and 0.32% for $X_{\text{CO}} = 0.4835$ and 0.2742, respectively.

^dThere are four data points. The predictions for two higher (lower) mole fractions X_{CO} disagree (agree) with experiment.

^eThe predicted angular position of the main rotational rainbow is outside the estimated experimental uncertainty.

^fThe phase of the interference oscillations is predicted correctly but the amplitude at $j = 5$ is not.

^gThe phase of the interference oscillations is not predicted correctly.

^hThe SAPT PES was not tested, but can be expected to match the experimental rate data easily.

Figure Captions.

FIG. 1: Angular dependence of the location, R_{tp} , of the repulsive wall corresponding to the turning point in the center-of-mass system for an elastic binary collision between Ne and CO at total relative energies $E = 200, 500, 800 \text{ cm}^{-1}$: results are shown for the XC(fit), S2, and SAPT PESs.

FIG. 2: State-to-state differential cross sections for Ne- $^{12}\text{C}^{16}\text{O}$ scattering for an average collision energy of 511 cm^{-1} for three PESs and experimental results from Ref. 20. In each panel, the experimental results have been scaled vertically to match the average integral cross section computed from the three surfaces. The calculated curves are identified as in Fig. 1.

FIG. 3: State-to-state relative product densities at 711 cm^{-1} and 797 cm^{-1} for S2 and XC(fit) $_{r=r_e}$ surfaces, and experimental results from Ref. 19. The vertical scale is arbitrary, but corresponds roughly to cross sections in \AA^2 computed on S2.

FIG. 4: Bottom panel: Integral cross sections $0 \rightarrow j_f$ transitions at 711 cm^{-1} for three PESs. The points from each surface are connected by lines to make it easier to follow the patterns. Top panel: density-to-flux factors $\langle g/v_f \rangle_{0j}$ computed for the XC(fit) $_{r=r_e}$ PES at 711 cm^{-1} , in which g is the relative speed of the colliders, v_f is the final laboratory-frame speed of the scattered molecule, and the angular brackets indicate a weighted average over the scattering angle in which the differential cross section is employed as the weighting function.

FIG. 5: Computed pressure broadening coefficients and experimental results for infrared fundamental and overtone lines. Experimental data for the 2-0 band are from Ref. 23. Data for the 1-0 band are from Ref. 24, except for the single point at $m = 25$ from Ref. 51. Points labeled “inelastic” were determined with Eq. (5). Points labeled “approx S-G” were determined with Eq. (6).

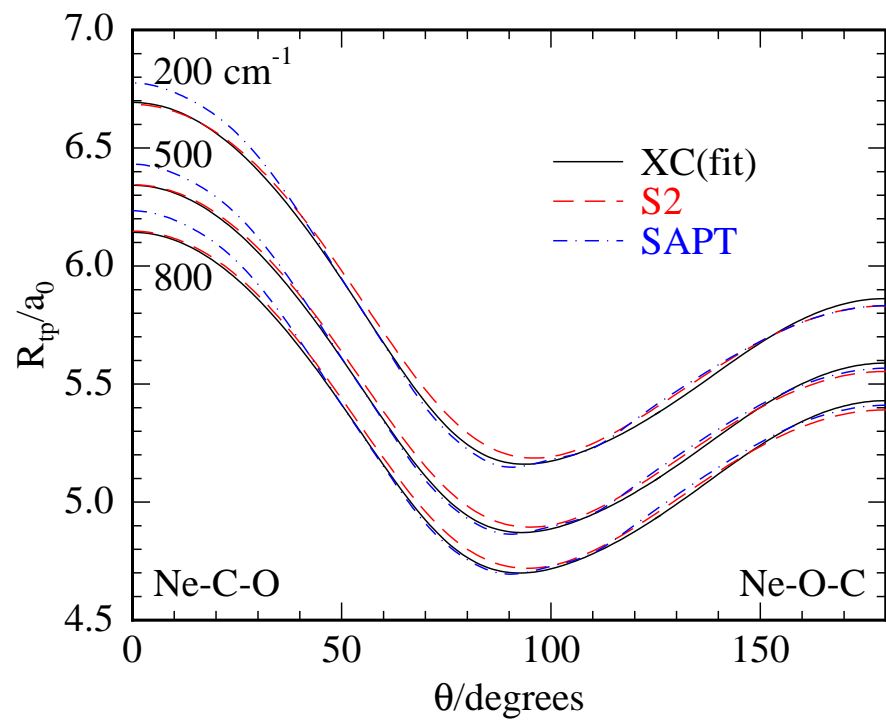


Figure 1.

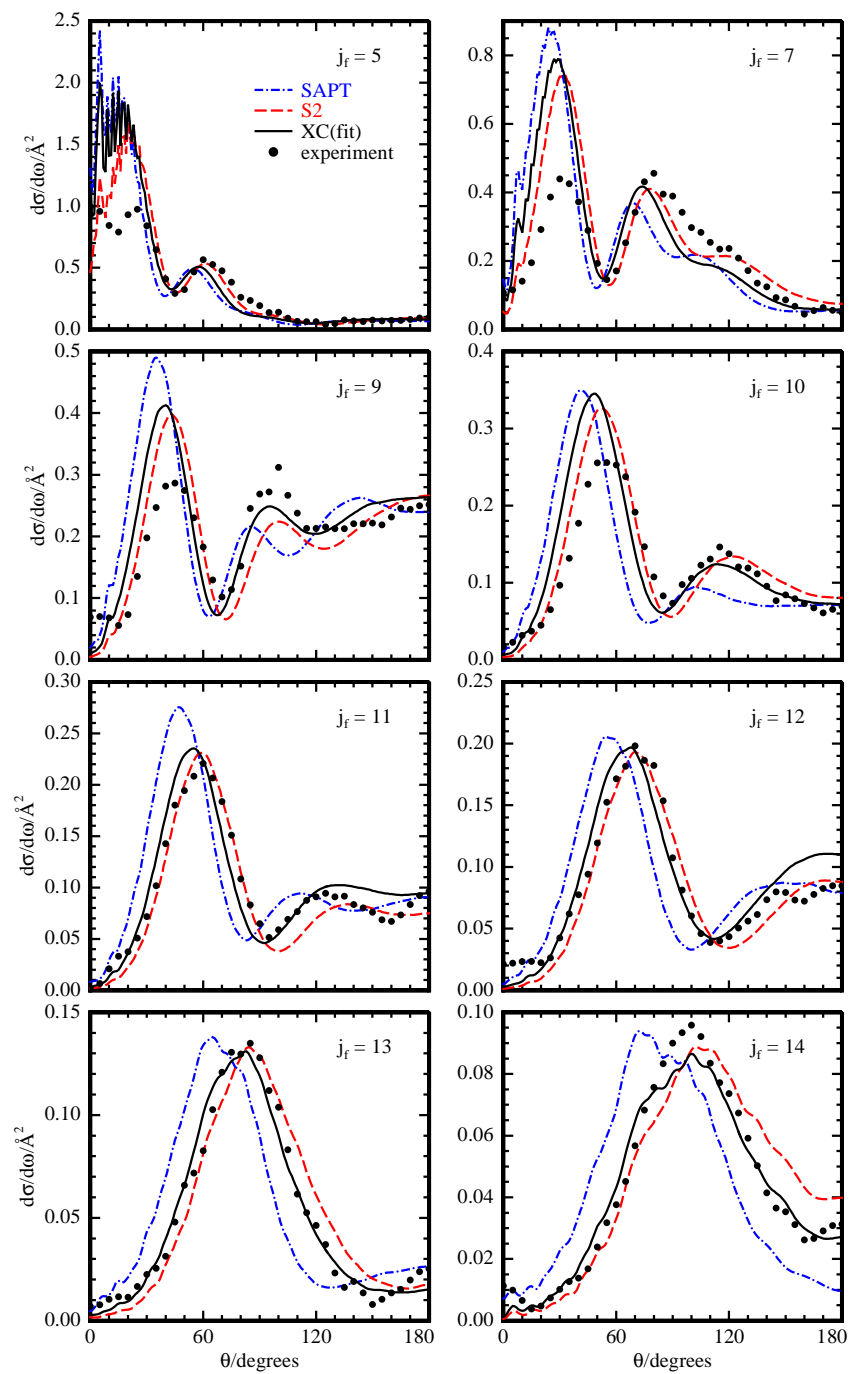


Figure 2.

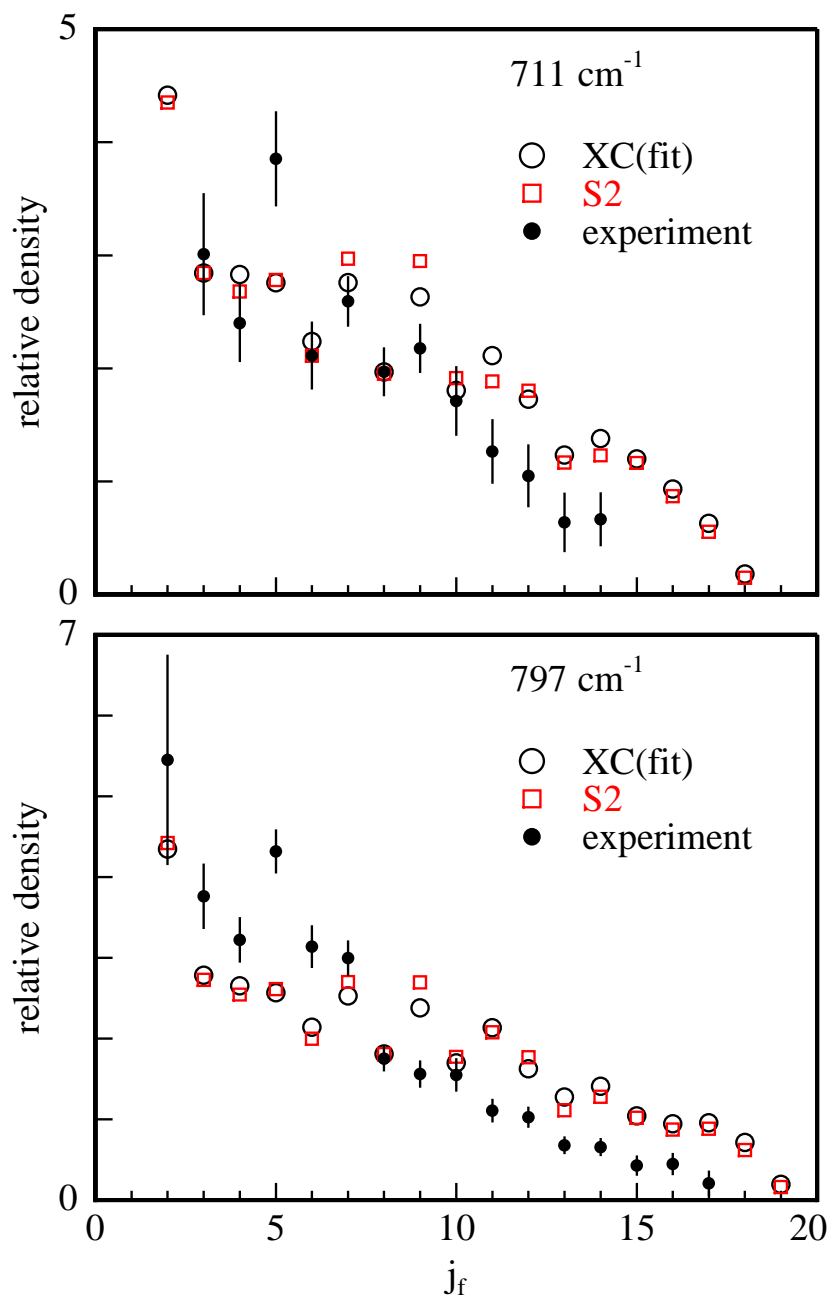


Figure 3.

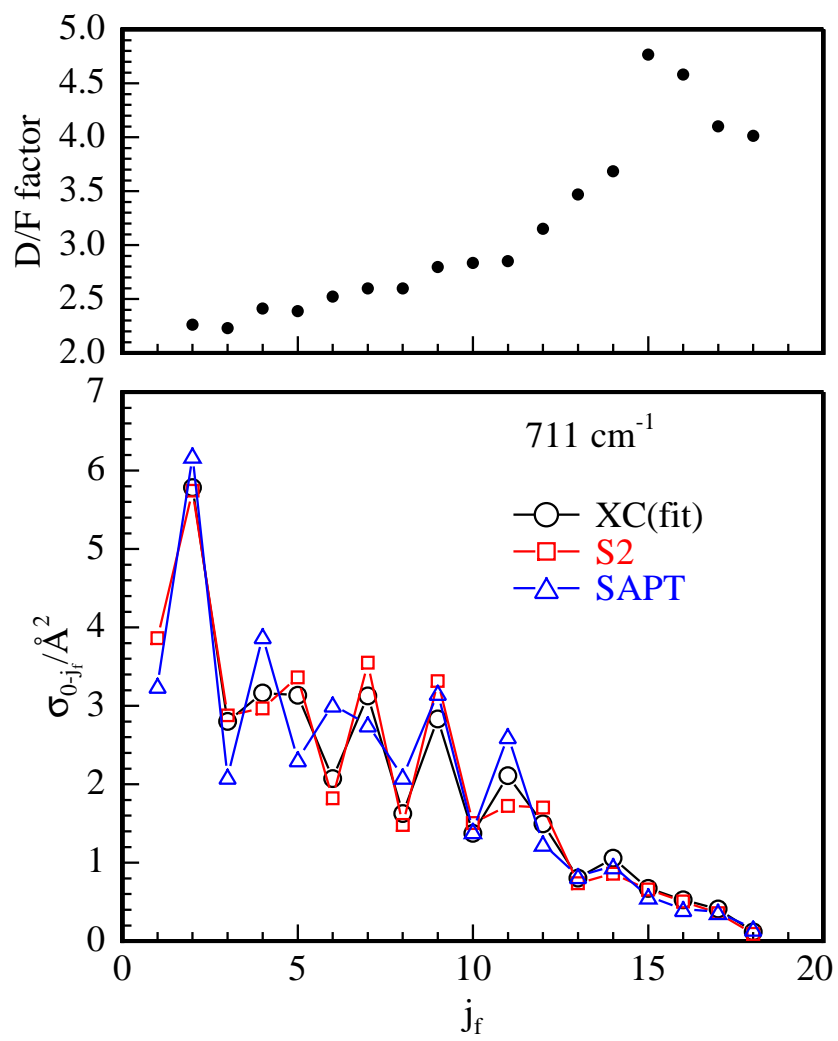


Figure 4.

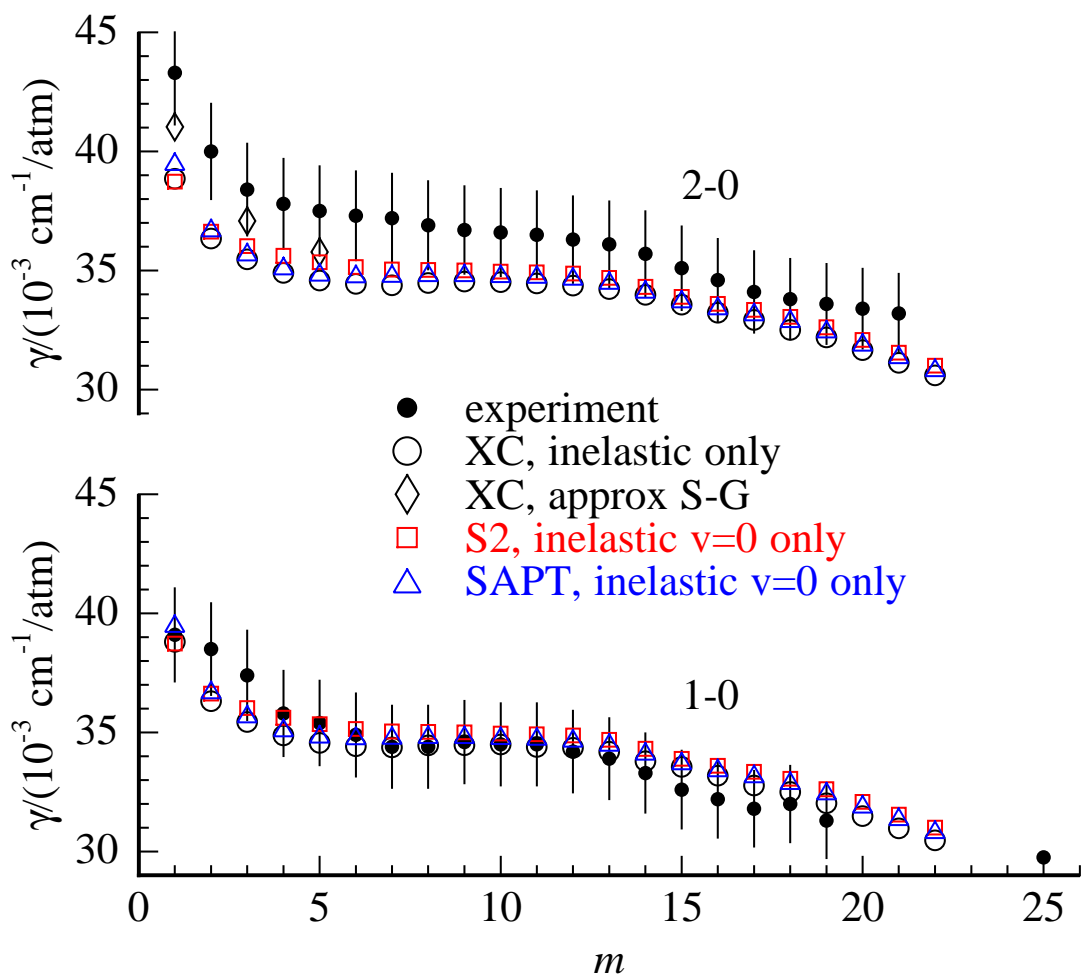


Figure 5.

-
- ¹ K.-C. Ng, W. J. Meath, and A. R. Allnatt, *Chem. Phys.* **32**, 175 (1978).
- ² K.-C. Ng, W. J. Meath, and A. R. Allnatt, *Mol. Phys.* **37**, 237 (1979).
- ³ W. J. Meath, D. J. Margoliash, B. L. Jhanwar, A. Koide, and G. D. Zeiss, in *Proceedings of the 14th Jerusalem Symposium on Quantum Chemistry and Biochemistry*, ed. B. Pullmann (Reidel, Dordrecht, 1981), pp. 101–115.
- ⁴ W. J. Meath and M. Koulis, *J. Mol. Struct.* **226**, 1 (1991).
- ⁵ R. J. Le Roy, C. Bissonnette, T. H. Wu, A. K. Dham, and W. J. Meath, *Faraday Disc.* **97**, 81 (1994).
- ⁶ A. K. Dham, F. R. W. McCourt and W. J. Meath, *J. Chem. Phys.* **103**, 8477 (1995).
- ⁷ C. Bissonnette, C. E. Chuaqui, K. G. Crowell, R. J. Le Roy, R. J. Wheatley, and W. J. Meath, *J. Chem. Phys.* **105**, 2639 (1996).
- ⁸ H. Wei, R. J. Le Roy, R. Wheatley, and W. J. Meath, *J. Chem. Phys.* **122**, 084321 (2005).
- ⁹ A. K. Dham, F. R. W. McCourt, and W. J. Meath, *J. Chem. Phys.* **130**, 244310 (2009).
- ¹⁰ K. A. Walker, T. Ogata, W. Jäger, M. C. L. Gerry and I. Ozier, *J. Chem. Phys.* **106**, 7519 (1997).
- ¹¹ G. Winnewisser, B. S. Dumesh, I. Pak, L. A. Surin, F. Lewen, D. A. Roth, and F. S. Rusin, *J. Mol. Spectrosc.* **192**, 243 (1998).
- ¹² D. A. Roth, I. Pak, L. A. Surin, B. S. Dumesh, and G. Winnewisser, *Z. Naturforsch. A*, **55**, 754 (2000).
- ¹³ L. A. Surin, A. V. Potapov, V. A. Panfilov, B. S. Dumesh and G. Winnewisser, *J. Mol. Spectrosc.* **230**, 149 (2005).

- ¹⁴ R. Moszynski, T. Korona, P. E. S. Wormer, and A. van der Avoird, *J. Phys. Chem. A* **101**, 4690 (1997).
- ¹⁵ G. C. McBane and S. M. Cybulski, *J. Chem. Phys.* **110**, 11734 (1999).
- ¹⁶ R. W. Randall, A. J. Cliffe, B. J. Howard and A. R. W. McKellar, *Mol. Phys.* **79**, 1113 (1993).
- ¹⁷ A. R. W. McKellar and M.-C. Chan, *Mol. Phys.* **93**, 253 (1998).
- ¹⁸ L. Monchick and E. A. Mason, *J. Chem. Phys.* **35**, 1676 (1961); E. A. Mason and L. Monchick, *J. Chem. Phys.* **36**, 1622 (1962).
- ¹⁹ S. Antonova, A. Lin, A. P. Tsakotellis, and G. C. McBane, *J. Chem. Phys.* **110**, 11742 (1999).
- ²⁰ K. T. Lorenz, D. W. Chandler, and G. C. McBane, *J. Phys. Chem. A* **106**, 1144 (2002).
- ²¹ R. B. Nerf, Jr., and M. A. Sonnenberg, *J. Mol. Spectrosc.* **58**, 474 (1975).
- ²² J.-M. Colmont, L. Nguyen, F. Rohart, and G. Wlodarczyk, *J. Molec. Spectrosc.* **246**, 86 (2007).
- ²³ J.-P. Bouanich, *J. Quant. Spectrosc. Radiat. Trans.* **12**, 1609 (1972).
- ²⁴ D. A. Draeger and D. Williams, *J. Opt. Soc. Am.* **58**, 1399 (1968).
- ²⁵ D. A. Hostutler, T. C. Smith, G. D. Hager, G. C. McBane, and M. C. Heaven, *J. Chem. Phys.* **120**, 7843 (2004).
- ²⁶ J. Brewer, *Determination of Mixed Viral Coefficients*, AFOSR Report # MRL-2915-C (1967); see also J. H. Dymond, K. N. Marsh, and R. C. Wilhoit, *Virial Coefficients of Mixtures*, in Landolt-Börnstein *New Series*, Group IV: Physical Chemistry, Vol. 21, *Virial Coefficients of Pure Gases and Mixtures*, Subvol. B, p. 64. Eds. M. Frenkel and K. N. Marsh. (Springer, Berlin, 2003).
- ²⁷ K. Vatter, H. J. Schmidt, E. Elias, and B. Schramm, *Ber. Bunsenges. Phys. Chemie* **100**, 73 (1996).
- ²⁸ R. D. Trengove, H. L. Robjohns, and P. J. Dunlop, *Ber. Bunsenges. Phys. Chem.* **88**, 450 (1984).

- ²⁹ J. Kestin, S. T. Ro, and W. A. Wakeham, *Ber. Bunsenges. Phys. Chem.* **86**, 753 (1982).
- ³⁰ N. Imaishi and J. Kestin, *Physica A*, **126**, 98 (1984).
- ³¹ A. Koide, W. J. Meath, and A. R. Allnatt, *Chem. Phys.* **58**, 105 (1981).
- ³² H. Kreek and W. J. Meath, *J. Chem. Phys.* **50**, 2289 (1969).
- ³³ A. Kumar and W. J. Meath, *Chem. Phys.* **189**, 467 (1994).
- ³⁴ W. J. Meath and A. Kumar, *Intl. J. Quantum Chem.* **S24**, 501 (1980).
- ³⁵ A. J. Thakkar, H. Hettema, and P. E. S. Wormer, *J. Chem. Phys.* **97**, 3252 (1992).
- ³⁶ H. Hettema, P. E. S. Wormer, and A. J. Thakkar, *Mol. Phys.* **80**, 533 (1993).
- ³⁷ J. M. Hutson and S. Green, MOLSCAT computer code, version 15 (1994); available at <http://www.giss.nasa.gov/tools/molscat>.
- ³⁸ M. H. Alexander and D. E. Manolopoulos, *J. Chem. Phys.* **86**, 2044 (1987).
- ³⁹ P. Brumer, *Chem. Phys. Lett.* **28**, 345 (1974).
- ⁴⁰ C. W. McCurdy and W. H. Miller, *J. Chem. Phys.* **67**, 463 (1977).
- ⁴¹ S. Antonova, A. Lin, A. P. Tsakotellis, and G. C. McBane, *J. Chem. Phys.* **110**, 2384 (1999).
- ⁴² D. Carty, A. Goddard, I. R. Sims, and I. W. M. Smith, *J. Chem. Phys.* **121**, 4671 (2004).
- ⁴³ F. R. W. McCourt, J. J. M. Beenakker, W. E. Köhler, and I. Kuščer, *Nonequilibrium Phenomena in Polyatomic Gases. 1. Dilute Gases* (Oxford University Press, Oxford, 1990).
- ⁴⁴ R. T. Pack, *J. Chem. Phys.* **78**, 7217 (1983).
- ⁴⁵ R. Moszynski, T. Korona, T. G. A. Heijmen, P. E. S. Wormer, A. van der Avoird, and B. Schramm, *Polish J. Chem.* **72**, 1479 (1998).
- ⁴⁶ G. C. McBane and P. Valiron, "PMP MOLSCAT", a parallel version of MOLSCAT version 14, available at <http://faculty.gvsu.edu/mcbaneg/pmpmolscat>.
- ⁴⁷ R. Shafer and R. G. Gordon, *J. Chem. Phys.* **58**, 5422 (1973).

- ⁴⁸ S. Green: PRBR_SAVE, an auxiliary program of the MOLSCAT computer code, available at <http://www.giss.nasa.gov/tools/molscat>.
- ⁴⁹ P. J. Davis and P. Rabinowitz, *Numerical Integration* (Blaisdell, Waltham, 1967).
- ⁵⁰ GCM is grateful to B. Stewart for pointing out this approach to finding the total classical cross section for a convex hard shell.
- ⁵¹ A. Henry, D. Hurtmann, M. MargottinMaclou, and A. Valentin, *J. Quant. Spectrosc. Rad. Transfer* **56**, 647 (1996).
- ⁵² A. S. Dickinson and M. S. Lee, *J. Phys. B* **18**, 3987 (1985).
- ⁵³ A. S. Dickinson and M. S. Lee, *J. Phys. B* **18**, 4177 (1985).
- ⁵⁴ A. S. Dickinson and M. S. Lee, *J. Phys. B* **19**, 3091 (1986).
- ⁵⁵ F. R. W. McCourt, J. J. M. Beenakker, W. E. Köhler, and I. Kuščer, *Nonequilibrium Phenomena in Polyatomic Gases. 2. Cross Sections, Scattering, and Rarefied Gases* (Oxford University Press, Oxford, 1992).
- ⁵⁶ H. O'Hara and F. J. Smith, *J. Comput. Phys.* **5**, 328 (1970).
- ⁵⁷ F. R. W. McCourt, *Gas Transport Properties*, Ch. 28 of *Handbook of Molecular Physics and Quantum Chemistry* Vol. 3 *Molecules in the Physico-chemical Environment: Spectroscopy, Dynamics and Bulk Properties*, Eds. S. Wilson, P. F. Bernath, and R. McWeeney, (Wiley, Chichester, 2003).
- ⁵⁸ G. C. Maitland, M. Rigby, E. B. Smith, and W. A. Wakeham, *Intermolecular Forces: Their Determination and Origin* (Clarendon Press, Oxford, 1981).
- ⁵⁹ A. K. Dham and S. C. Gupta, *J. Phys. B* **9**, L127 (1976).
- ⁶⁰ K. Singh, A. K. Dham, and S. C. Gupta, *J. Phys. B* **25**, 679 (1992).
- ⁶¹ R. A. Aziz, W. J. Meath, and A. R. Allnatt, *Chem. Phys.* **78**, 295 (1983).

- ⁶² A. van der Pol, A. van der Avoird, and P. E. S. Wormer, *J. Chem. Phys.* **92**, 7498 (1990).
- ⁶³ E. A. Mason, *J. Chem. Phys.* **27**, 75 (1957).
- ⁶⁴ T. S. Storvic and E. A. Mason, *J. Chem. Phys.* **45**, 3752 (1966).
- ⁶⁵ A. K. Dham and S. C. Gupta, *J. Phys. B* **8**, 2898 (1975).
- ⁶⁶ A. K. Dham and W. J. Meath, *Chem. Phys.* **196**, 125 (1995).
- ⁶⁷ Expressions for the polarization factors $f_{02\eta} = 1 + \psi_{02}$ and $f_{12\lambda} = 1 + 5\psi_{12}/3$ can be obtained by using Eqs. (7.1-24) and (7.2-7b) of Ref. 43 for ψ_{02} and ψ_{12} , respectively.
- ⁶⁸ A. K. Dham, W. J. Meath, J. W. Jechow, and F. R. W. McCourt, *J. Chem. Phys.* **124**, 034308 (2006).
- ⁶⁹ A. K. Dham, F. R. W. McCourt, and A. S. Dickinson, *J. Chem. Phys.* **127** 054302 (2007).
- ⁷⁰ S. Chapman and T. G. Cowling, *The Mathematical Theory of Nonuniform Gases*, 3rd Edition (Cambridge University Press, Cambridge, 1970).
- ⁷¹ F. R. W. McCourt, *Mol. Phys.* **101**, 2181 (2003).
- ⁷² F. R. W. McCourt, *Mol. Phys.* **101**, 2409 (2003).
- ⁷³ F. R. W. McCourt, D. Weir, G. B. Clark, and M. Thachuk, *Mol. Phys.* **103**, 17 (2005).
- ⁷⁴ F. R. W. McCourt, D. Weir, M. Thachuk, and G. B. Clark, *Mol. Phys.* **103**, 45 (2005).
- ⁷⁵ S. Chapman, *Phil. Trans. Roy. Soc. A*, **217**, 115 (1917).
- ⁷⁶ P. S. Arora, J. M. Symons, M. L. Martin, and P. J. Dunlop, *Chem. Phys. Letters* **62**, 396 (1979).
- ⁷⁷ R. D. Trengove, H. L. Robjohns, and P. J. Dunlop, *Ber. Bunsenges. Phys. Chem.* **88**, 450 (1984).
- ⁷⁸ W. L. Taylor and P. T. Pickett, *Intl. J. Thermophys.* **7**, 837 (1986).
- ⁷⁹ W. L. Taylor, *J. Chem. Phys.* **105**, 8333 (1996).
- ⁸⁰ A. K. Dham and W. J. Meath, *Mol. Phys.* **88**, 339 (1996).
- ⁸¹ R. A. Aziz, M. J. Slaman, A. Koide, A. R. Allnatt, and W. J. Meath, *Mol. Phys.* **77**, 321 (1992).

⁸² A. K. Dham and W. J. Meath, *Mol. Phys.* **99**, 991 (2001).

⁸³ K. Watanabe, A. R. Allnatt, and W. J. Meath, *Chem. Phys.* **68**, 423 (1982).